Resolution of the size/distance degeneracy of the dust devils signals observed with a stationary meteorological station

Running Head: Resolution of the dust devil signals degeneracy

Key words: Dust Devils; Micrometeorology; Earth; Mars; Depth Reconstruction (from a single still image)

Abstract

The monitoring of dust devils using only a meteorological station is limited by the size/distance degeneracy that affects the acquired time series. It is not possible to retrieve directly information on their morphology, translational motion, distance of passage and vortex intrinsic parameters as the core pressure drop and maxima rotational speed.

We propose a simple model to estimate the distance of passage (commonly referred to as *impact parameter*) of the dust devils encounters from the station, monitored using a 2D anemometer. Our technique is based on the study of an easily recognizable feature of the signal trend, univocally connected to the vortex distance of passage.

In order to test the model, we have analyzed the measurements acquired during a Sahara field campaign. Our meteorological station was equipped with a camera, to compare the modeled distances with the ones obtained from the images. For all the acquired events the experimental results are in good agreement with the model. Overall, we observed dust devils passing between 3 m and 150 m from the station, assessing the reliability of the technique over a wide range of distances.

The evaluation of the impact parameter allows to fully characterize the meteorological encounters and to retrieve the vortex intrinsic parameters. The simplicity of the procedure makes it a powerful tool in the study of the relations among different vortex features (e.g., dust concentration and induced electric field) and their dependence on the distance from the station, easily applicable to past and future terrestrial and martian surveys.

1. Introduction

1.1 Dust Devils

Dust devils are convective vortices, stable columns of air in rotary motion, strong enough to entrain material from the surface. Sinclair has been the first to report the general characteristics of these whirlwinds by studying a large dust devil dataset observed in the Sonoran Desert (Arizona) (Sinclair 1964; Sinclair 1969; Sinclair 1973). The diameter of the dust column can be roughly constant or increase with the height, and the vortex can be perpendicular to the surface or slightly tilted in the direction of motion. It has been shown (e.g., Balme and Greeley, 2006; Murphy et al. 2016) that strong insolation, low humidity, lack of high obstacles, and gently sloping topography are all advantageous conditions for the formation of such vortices. The whirling nature arises from regions of strong temperature gradients that could lead to the generation of the convection motion and pressure gradient. Indeed, the horizontal rotary motion is due to the presence of a low-pressure core. Let us call v_r the rotational speed (see Table 1 for the complete list of the symbols used in the paper). Its dependence over the distance d from the center of the vortex can be approximated by the Rankine vortex model (see e.g. Rankine 1901; Giaiotti and Stel 2006):

$$v_r(d) = \begin{cases} V_r \dfrac{R}{d} & if\ d > R \quad (1a) \\ V_r \dfrac{d}{R} & if\ d < R \quad (1b) \end{cases}$$

where R is radius of the vortex. Eq. (1) shows that as d increases v_r increases, until it reaches its maximum V_r in d = R. The region identified by d = R is known as *vortex wall*. Further increase of d decreases v_r.

One can also prove that, when the signal is acquired by a stationary meteorological station, the dependence of the pressure P on d follows a Lorentzian curve (Ellehoj et al. 2010):

$$P(d) = \frac{-\Delta P_o}{1 + \left(\frac{d}{\mathrm{R}}\right)^2} + B \quad (2)$$

where B and $\Delta P_o \equiv B - P(d = 0)$ are the background pressure and the magnitude of the pressure drop in $d = 0$. The most common type of dust devils has one single pressure core and the magnitude of ΔP_o is usually of the order of one thousandth of the atmospheric pressure (~1 mbar on Earth) (e.g. Balme and Greeley, 2006; Murphy et al., 2016).

In d = R, when the vortex is in a steady state we can assume the cyclostrophic balance, i.e., the force due to the gradient in pressure equates the centrifugal force:

$$\frac{{V_r}^2}{R} = \frac{\Delta P_o}{\rho} \tag{3}$$

where ρ is the density of the air.

The motion of the dust devils is the sum of a translational motion, a rotation around the vertical axis and a vertical motion due to the convection. The combined effect of these flow motions, in addition to pressure-gradient force (Klose et al., 2016), makes the dust devils one of the most efficient phenomena for entraining grains into the atmosphere, in particular in the dust size range (Greeley et al., 2003, Neakrase et al., 2016). Dust devils can start dust grain lifting with a wind speed lower than the one required by the unidirectional winds of gusts and dust storms.

On Earth, the whirlwinds can heavily affect the atmospheric dust concentration on local scale. However, this phenomenon is not limited to the terrestrial environment and several planetary missions have shown the occurrence of dust devil lifting phenomena on Mars. Mars is an active planet from the aeolian point of view, with frequent sand and dust mobilization events (Bourke et al., 2008; Silvestro et al. 2010; Silvestro et al. 2015). The nearly global coverage of Mars obtained by orbital cameras such as the NASA Mars Orbital Camera on the Mars Global Surveyor mission, and the ESA High Resolution Stereo Camera on the Mars Express mission, have shown that these vortices are highly diffused on the planet. Dust devils have been observed in both hemispheres, almost at every latitudes and elevation, over the whole martian year (Edgett and Malin, 2000; Malin and Edgett, 2001; Greeley et al., 2004; Stanzel et al., 2008). The dust devils formed on Mars are larger in size when compared to those formed on the Earth. However, the meteorological properties are very similar,

suggesting how the underlying dynamics and formation mechanism may have common foundations (Ringrose et al., 2003; Franzese et al., 2018).

Many studies have aimed to assess the impact that dust devils have on the climate of Mars. Overall, they appear to account for ~50% of the global dust budget (Ferri et al., 2003; Whelley & Greeley, 2008; Guzewich et al., 2015). Also, dust devils have been indicated as principal sustaining mechanism for the Martian atmospheric dust haze, in particular outside the dust storm season (Neubauer, 1966; Thomas and Gierasch, 1985; Murphy et Nelly., 2002; Ferri et al., 2003; Fisher et al., 2005; Cantor et al. 2006). In addition, the mobilized grains tend to charge by collisions and the triboelectrification can induce strong electric fields (see Harrison et al. 2016 for a review on the topic). This variation of the atmospheric electricity can enhance the formation of oxidants able to scavenge organic material from the surface (Atreya et al., 2006). Potentially, the electric field induced by the dust devils can overcome the martian electric breakdown (Farrell et al., 2017; Franzese et al., 2018), leading to the formation of discharges able to affect the atmospheric chemistry and also interfere with the operations of the surface instruments in space missions.

For these reasons, dust devils are an important factor in the study of the martian climate. They will be subject of specific study during the current and next martian surface exploration missions, such as NASA Insight, successfully landed on November 2018, and ESA/ROSCOSMOS ExoMars 2020.

$\boldsymbol{b}$	average background wind velocity
θ_b	direction of the vector $\boldsymbol{b}$
$\boldsymbol{d}$	distance of the dust devil from the meteorological station
θ_d	direction of the vector $\boldsymbol{d}$
$\boldsymbol{d_o}$	impact parameter: minimum distance of the dust devil from the station
θ_{do}	direction of the vector $\boldsymbol{d_o}$, we will put $\vartheta_{do} = ½\ \pi$
$f(d)$	generic function that describes the dependence on distance of the q signature
ΔP_o	pressure drop at the vortex core

q	generic meteorological feature of the vortex monitored by the station
q_o	intrinsic variation of the quantity q
Δq_{Max}	maximum measured variation of the quantity q
R	vortex radius
$\boldsymbol{s}$	vortex translational velocity
θ_s	direction of the vector $\boldsymbol{s}$
t_o	time instant when the vortex reaches the distance d_o, we will put $t_o=0$
$\boldsymbol{v_r}$	vortex rotatory wind speed
θ_{vr}	direction of the vector $\boldsymbol{v_r}$
V_r	maximum rotatory wind speed (reached at the vortex wall)
$\boldsymbol{v_t}$	total wind speed measured by the meteorological station
θ_{vt}	direction of the vector $\boldsymbol{v_t}$
w	maximum rotatory wind speed measured by the meteorological station

Table 1 List of the symbols used in the paper. All the directions are evaluated respect to the *x*-axis of the instrument frame.

1.2 The problem of the degeneracy size/distance

We introduce here two different frames: the rest frame of the meteorological station (*instrument frame*) and the vortex proper frame, comoving with the dust devil and centered on it (*dust devil frame*). Let us define q as a generic physical quantity monitored by our station, and q_o its variation due the passage of the vortex, i.e. the variation observable in the dust devil frame. By definition, q_o is independent from the distance d. It is related to the proper characteristics of the vortex (e.g. its size R) and is directly measurable only if the vortex passes directly over the instruments.

Eqs. (1) and (2) describe the trend of the pressure and of the wind velocity expected during a dust devil encounter. In case of P, q_o represents the pressure drop at the vortex core (ΔP_o). In case of the rotational wind speed q_o represents the rotation at the vortex wall, V_r.

In the dust devil frame, *q(d)* is simply a constant: $q(d) = q_o + B$; where *B* is the background value. Here we are considering a dust devil in a stable condition, where q_o is constant in time and *B* is constant and spatially uniform. In the instrument frame, we have to consider the effect of the motion of the dust devil and *q(d)* can be written as:

$$q(d) = q_o\, f(d) + B \quad \textbf{(4)}$$

where the function *f(d)* expresses how the value of the induced variation decreases with distance and *B* is the background value in the new system.

During its motion, the dust devil reach a minimum distance from the station d_o (the impact parameter) usually greater than zero. The maximum variation of the signal in the instruments frame, Δq_{Max}, is obtained in the point of minimum approach:

$$\Delta q_{Max} = \Delta q(d_o) = q_o\, f(d_o) \quad \textbf{(5)}$$

We can measure Δq_{Max} directly. However, using only Δq_{Max} it is impossible to derive q_o, the function *f(d)* and the value of d_o: that is, it is not possible to completely characterize the observed dust devil. This leads to the degeneracy size/distance of the measure: i.e., a small dust devil passing near the station (low R and d_o) or a large one passing farther away from the station (larger R and d_o) can in principle give rise to the same signals *q(t)* and Δq_{Max}. Another source of ambiguity is the vortex sense of rotation, which is also not directly inferable using the acquired signals.

The various physical quantities scale differently with the distance from the vortex. In case of the pressure and wind rotational speed, the form of $f(d)$ is already known in literature, being it a linear function (eq. (1)), and a Lorentzian (eq.(2)), respectively. Studying the distribution of a single parameter q whose dependence on distance $f(d)$ is already given, the impact parameter can be marginalized starting from a statistically significant number of encounters and supposing a random statistical distribution of the passage distances. This approach is commonly used in literature, both for terrestrial and martian dust devils surveys. However, in most of the cases, we ignore the form of q_o and *f(d)* and we are unable to empirically investigate them using the acquired signals *q(t)*, due to

144 the size/distance degeneracy. In addition, in order to improve our knowledge on the physics of the
145 whirlwinds, it is necessary to study the relations among the different vortex parameters. This is not
146 possible ignoring how each scales with the distance.
147 Franzese et al. 2018, have presented the first statistical analysis of the electric proprieties of the dust
148 devils, observing how the electric signature is strictly connected to the measured pressure drop,
149 horizontal and vertical wind speed and dust concentration. The results are affected by strong
150 uncertainties, mainly due to the size/distance degeneracy. This kind of studies has motivated the
151 development of techniques to estimate the impact parameters of the dust devil encounters with a
152 stationary meteorological station.
153 Lorenz, 2016 has addressed the problem proposing a model to study the acquired dust devils
154 signatures and a heuristic estimation of the intrinsic and geometrical parameters of the encounters
155 (impact parameter, size, core pressure drop and wall rotatory speed). In order to retrieve these
156 parameters, the procedure involves a global fitting of the measured pressure, wind speed and direction
157 time series. However, ambiguities remain in discriminating the more significant fit result.
158 In order to find a direct approach and fully resolve the degeneration, we developed a new technique
159 to evaluate the distance between the acquiring station and the passing whirlwind by analyzing the
160 induced wind speed and direction variation.
161 To validate the model, we performed a field campaign coupling the meteorological instruments with
162 a camera. In this work, we compare the results obtained using our model with the ones obtained
163 directly from the images of the events. This campaign is part of a series of field surveys performed
164 in the frame of development of the DREAMS station, on board of the ESA/Roscosmos ExoMars 2016
165 mission, and of the MicroMED sensor, which will be on board of the ESA/Roscosmos ExoMars 2020
166 (Esposito et al. 2016; Aguirre et al. 2017; Esposito et al. 2018).

1. Methods

1.1 Equipment

In July 2017 we performed a field campaign in the Sahara Desert of the Tafilalt region (Morocco). The chosen site is placed along the dry bed of Ziz river, at coordinates: -4. 1226° W, 31. 1488° N (see Fig. 1 and Fig. 2).

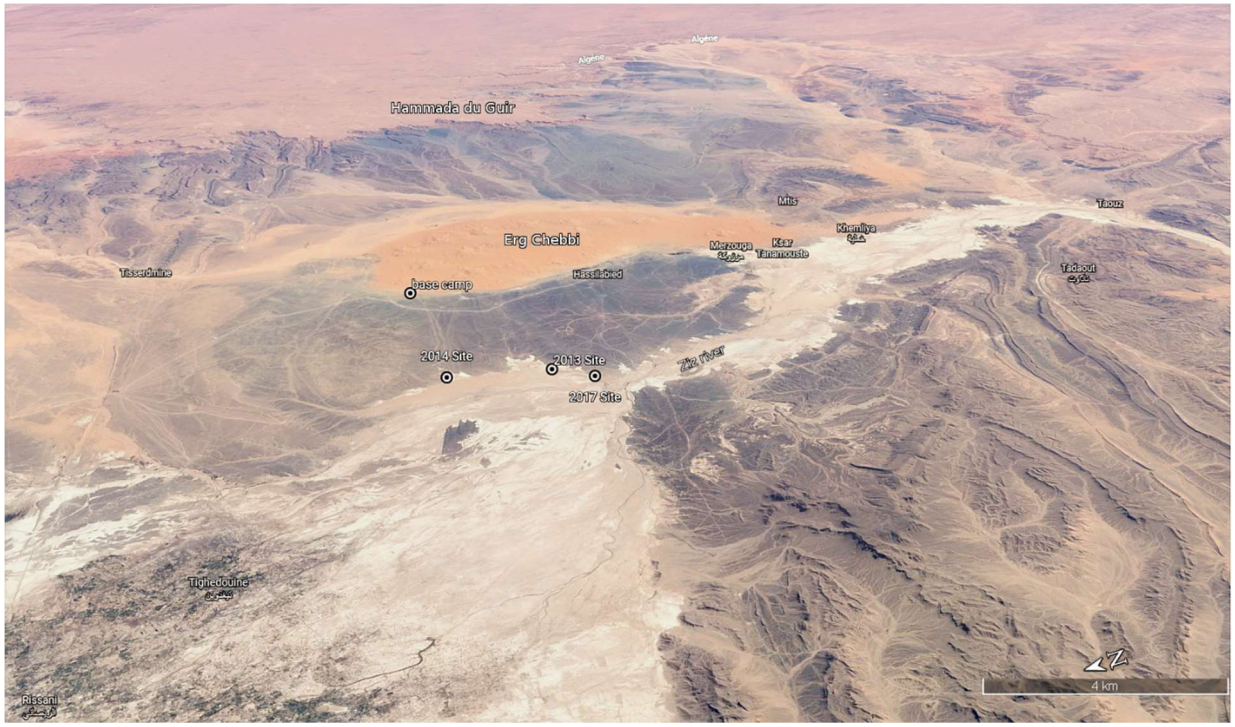

Fig. 1 *The field campaign sites in the Tafilalt region (Morocco). (source: Google Earth)*

Fig. 2 *A close up of the soil at the measuring site*

We deployed a fully equipped meteorological station, mounted on a principal mast. We coupled it with a single camera system, hosted on a separate mast placed few meters away (see Fig. 3). The meteorological station included:

- three 2d anemometers (Gill WindSonic) at 0.7 m, 2.0 m and 3.35 m;
- three thermometers placed at different height from the ground. The first at 0.1 m below the surface, with a soil humidity sensor (CS616-C), and the second right under the surface. The last at 1.70 m above the ground, coupled with an air humidity sensor.
- a solar irradiance sensor (LI-COR LI-200 Pyranometer) at 0.3 m;
- an atmospheric pressure sensor (Vaisala Barocap PTB110) at ground level;
- one Sensit sensor (instrument to monitor the saltation activity) placed 2.70 m away from station center.

The camera was oriented in order to catch the first mast and the passing dust events in the same image with a field of view of about 130°.

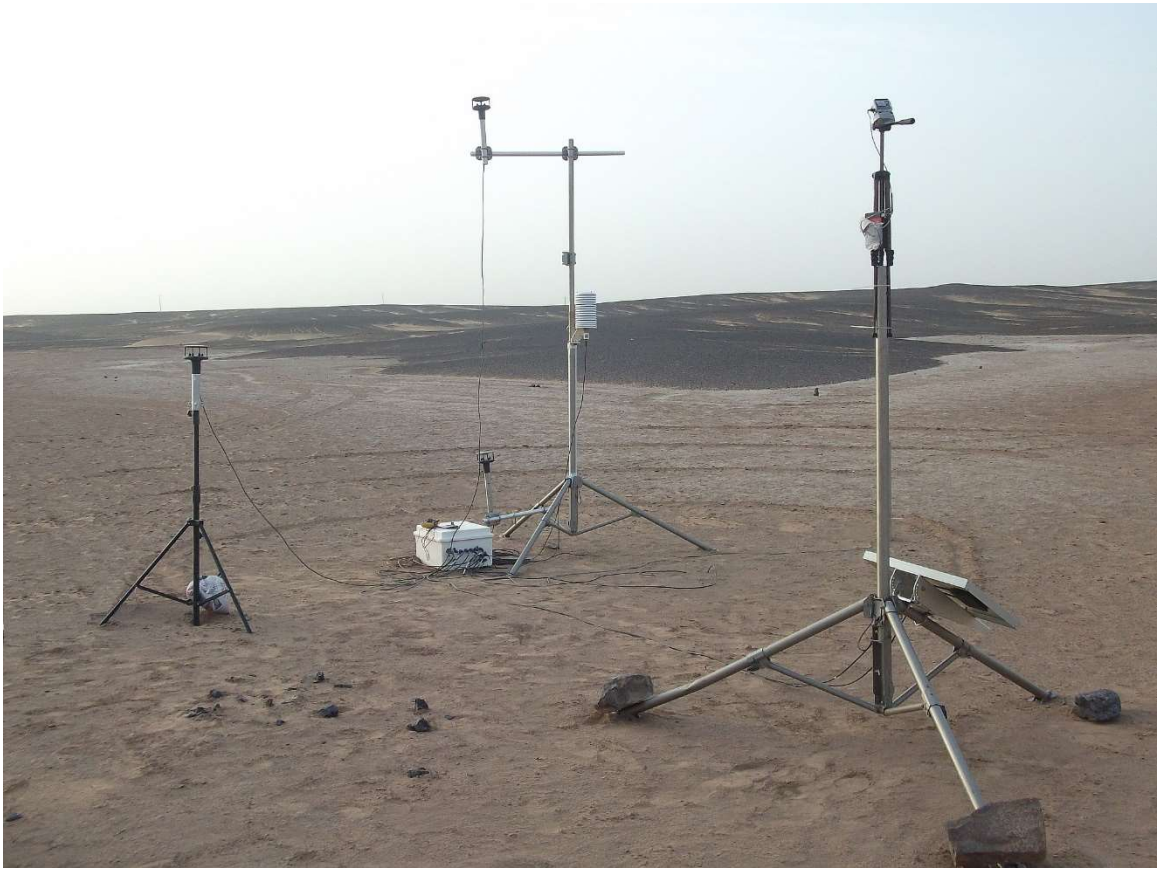

Fig. 3 ***The station deployed during the field campaign. The principal mast is equipped with two anemometers, a thermometer, a pressure sensor and a solar irradiance sensor. A third anemometer is placed on a separate tripod. The camera system and the solar panel are hosted on a secondary mast. We installed also two thermometers, for the superficial and sub-superficial temperature, and a Sensit impact sensor.***

We have acquired the meteorological during day and night at 2 Hz rate. Camera images have been acquired during day time only at the same rate. Data were acquired from the 21th July to the 24th July 2017.

For the purposes of this paper we will focus only on the wind speed and direction data and on the synchronous camera acquisitions.

1.2 Wind signature model

As discussed in the introduction, the induced variation Δq_{Max} of a generic signal $q(t)$ is the easiest quantity to measure. However, Δq_{Max} depends on both q_o and d_o (eq.(5)). We hence start by studying the wind speed signal $q(t)$ (eq. (1)), in order to find another measurable quantity depending on just one of the two factors.

The maximum value (V_r) of the rotary speed and R are intrinsic parameters of the dust devil. Note that for fully formed and stable vortices, the ones we are interested in, we can consider V_r and R to be fixed. The varying parameters are those related to the relative motion of the dust devil with the observation point, such as d and the measured $\mathbf{v}_r$. The vortex translates advected by the wind background. This implies that its traverse velocity $\boldsymbol{s}$ closely matches the average background wind speed $\boldsymbol{b}$, both in terms of magnitude and direction $(\boldsymbol{b \cong s})$ (e.g. Balme et al. 2012). Dust devils may follow paths that are not strictly straight. Nonetheless, considering the short average duration of the encounter (Franzese et al., 2018), the motion can be we approximated as linear uniform with parameters: $s = b$ and $\theta_s = \theta_b$.

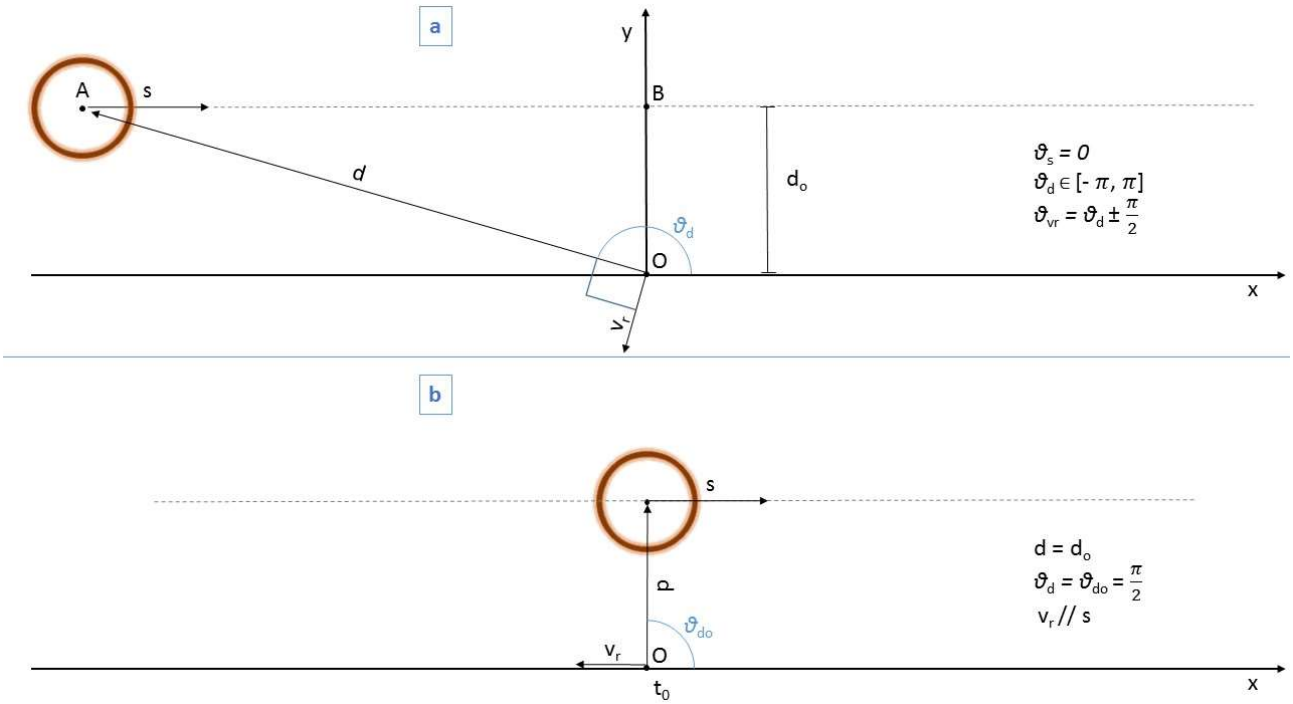

Fig. 4 *Schematization of a dust devil passage. The chosen reference frame has the x axes parallel to the vortex travel speed s. In a) the vortex still far from the station; in b) the vortex at the minimum distance from the instruments. Notice how* $v_r \perp \mathbf{d}$*, from which it follows* $\theta_{vr} = \theta_d \pm \frac{\pi}{2}$ *(± depending on the sense of rotation).*

The center of the instrument frame O_{xy} (see Fig. 4) is on the meteorological station. Without losing generality, we choose the *x*-axis to be parallel to the translational velocity $\boldsymbol{s}$ of the vortex, directed along the dust devil motion. Being $x \parallel s$, the direction of *s* is $\theta_s = 0$. $\boldsymbol{d}$ is the vector position of the center of the vortex in O_{xy}, with θ_d its direction. Its dependence on the time *t* can be written as:

$$d^2 = s^2\, t^2 + {d_o}^2 \tag{6}$$

which in components is:

$$\begin{cases} d_x = s\cos(\theta_s)\, t + d_{ox} \\ d_y = s\,\mathrm{sen}(\theta_s)\, t + d_{oy} \end{cases} \tag{7}$$

where *t* is the time variable, $t \in [-\infty, +\infty]$ while $d \in [-\infty, d_o] \cup [d_o\ +\infty]$. In particular, the minimum $\boldsymbol{d_o}$ of $\boldsymbol{d}$ is usually referred to as impact parameter. Following the convention introduced in Fig. 4b), $\boldsymbol{d_o}$ is reached at $t \equiv t_0 = 0$ and is directed along $\theta_{do} = \frac{\pi}{2}$. When $\boldsymbol{d} \equiv \boldsymbol{d_0}$, $d \perp s$, while the direction of the vortex rotation will determine if $\boldsymbol{s}$ and $\mathbf{v}_r$ are parallel or antiparallel. We are going to consider both scenarios, as in literature these cases are both likely to happen. We will define a rotation "discordant" if *s* and v_r are antiparallel at $t = t_o$, and "concordant" otherwise.

The wind speed measured in *O* is the sum of $\boldsymbol{b}$ and of $\mathbf{v}$. Let's us call this sum the total wind speed ($\mathbf{v}_t$), in terms of its dependence on the distance from *O* we have:

$$\mathbf{v_t}(d) = \mathbf{s} + \mathbf{v_r}(d) \tag{8}$$

In the above equation, we have not explicated the dependence of $\mathbf{v}_r$ on *R*, for the only purpose of simplifying the notation. However, *R* will still appear in our calculations, as it should. We can rewrite eq. (8) in terms of its components:

$$\mathrm{v}_{tx}(d) = \mathrm{s}\, cos(\theta_s) + \mathrm{v}_r(d)\, cos(\theta_{vr}) \tag{9}$$

$$\mathrm{v}_{ty}(d) = s\, sin(\theta_s) + \mathrm{v}_r(d)\, sin(\theta_{vr}) \tag{10}$$

For its direction θ_{vt} we get:

$$\theta_{vt}(d) = \arctan\left(\frac{\mathrm{v}_{ty}(d)}{\mathrm{v}_{tx}(d)}\right) \quad \textbf{(11)}$$

We can also derive a relation between the direction of ***d,*** its direction and the impact parameter. From the triangle OAB defined in Fig. 4a) we see that:

$$d_o = d\cos(\theta_d - \theta_{do}) \quad \textbf{(12)}$$

from which it follows:

$$\cos(\theta_d - \theta_{do}) = \frac{d_o}{d} \quad \textbf{(13)}$$

$$\sin(\theta_d - \theta_{do}) = \sqrt{1 - \left(\frac{d_o}{d}\right)^2} \quad \textbf{(14)}$$

We also define the quantity *w* as the maximum value of the rotational speed measured in *O*. In the case of non-direct passage we have that $w = \mathrm{v}_r(d_o) = V_r\frac{R}{d_o}$, while, in case of direct passage, *w* simply coincides with V_r.

Depending on the magnitude of d_o we can divide the events in two categories:

- the case of direct passage, where the dust devils pass over the station ($d_o \leq R$) ;
- and the case of non-direct passage ($d_o > R$), for the dust devils passing outside the station.

In the following subsections we will present the case of non-direct passage. The case of direct passage is presented for completeness in Appendix-A. Indeed, this latter case represents a very small percentage of the dust devils encounters. In addition, the passage of the vortex over the instruments already partially resolve the degeneracy, allowing the direct measurements of some of the intrinsic parameters.

As noted, in $d = d_0$ we can have $\boldsymbol{s}$ and $\mathbf{v}_r$ either parallel or antiparallel, hence a concordant or a discordant rotation. Both cases are equally probable and has to be analyzed separately. We will show that, despite the two different geometry of the vortex passage, the method that we are proposing remains unaltered.

1.2.1 Concordant Rotation

Given our definition, a concordant rotation satisfies the relation:

$$\theta_{vr} = \theta_d - \frac{\pi}{2} \tag{15}$$

In addition, $d \perp v_r \; \forall t$. From Fig. 4b we know that $\theta_{do} = \frac{\pi}{2}$. Hence, using eqs.(9), (13) and (15) we get:

$$\mathrm{v}_{tx}(d) = s + \mathrm{v}_r(d)\,\frac{d_o}{d} \tag{16}$$

while it follows from eqs. (10), (14) and (15):

$$\mathrm{v}_{ty}(d) = \mathrm{v}_r(d)\sqrt{1 - \left(\frac{d_o}{d}\right)^2} \tag{17}$$

For a dust devils passing outside the meteorological station ($d_o > R$), substituting the eq.(1a) in eq.(16) and eq.(17), the functions $\mathrm{v}_{tx}(d)$ and $\mathrm{v}_{ty}(d)$ became:

$$\mathrm{v}_{tx}(d) = s + V_r\frac{R\;d_o}{d^2} \tag{18}$$

$$\mathrm{v}_{ty}(d) = V_r\frac{R}{d}\;\sqrt{1 - \left(\frac{d_o}{d}\right)^2} \tag{19}$$

$\mathrm{v}_{ty}(d)$ (eq. (19)) has 4 critical points: $d = \pm\sqrt{2}\,d_o$ and $d = \pm\infty$, while $\mathrm{v}_{tx}(d)$ (eq. (18)) has one global maximum in $d = d_o$ and two minima in $d = \pm\infty$. The trend at infinite distance is not of interest for us, hence we will neglect $d = \pm\infty$ in the remaining.

With the above results and eq. (6), we can see that the maximum and minimum of v_{ty} are reached for $t = \pm\frac{d_o}{s}$, i.e. their position does not depend on *R* and V_r. We have hence accomplished the initial purpose of our analysis: we have found a quantity that depends only on *s* and d_o, and not on the intrinsic characteristics (radius, rotatory velocity at vortex wall, core pressure drop) of the dust devil.

The situation is slightly different for the direction $\theta_{vt}(d)$. Its stationary points are for $d = \pm\frac{d_o\sqrt{2s+w}}{\sqrt{s}}$. Substituting for t, we get $t = \pm\frac{d_o\sqrt{s+w}}{\sqrt{s^3}}$. The latter depends on *w*, which is function both of V_r and R, hence is not directly useful for the resolution of the degeneracy. However, we will describe in section 1.2.3 how to find an approximated value for *w* from the wind time series.

As an example, we show in Fig. 5 the total velocity $\mathbf{v_t}(t)$, its components $\mathrm{v}_{tx}(t)$ and $\mathrm{v}_{ty}(t)$, and direction $\theta_{vt}(t)$ of a vortex with intrinsic parameter equal to V_r = 25 m/s and R = 3 m, and with s = 5 m/s and d_o = 4.5 m. Fig. 5 a) shows that as *t* approaches 0 (that is, as the vortex gets close to the meteorological station) $\mathrm{v}_t(t)$ approaches $s + w$, in accordance to our previous results. Similarly, in Fig. 5 b) we can see that $\mathrm{v}_{tx}(t)$ also reaches a maximum in t = 0, but the peak is narrower. As expected, the trends of $\mathrm{v}_{ty}(t)$ and $\theta_{vt}(t)$ exhibit both a maximum and a minimum, Fig. 5 c) and Fig. 5 d). We point out here that in the case of a concordant rotation the maximum precedes the minimum: we will see in par. **Errore. L'origine riferimento non è stata trovata.** that this is not the case for a discordant rotation, and we can then use this feature to identify the direction of the rotation.

To show the independence of $\mathrm{v}_{ty}(t)$ stationary points from its intrinsic parameters, we have also plot in red the signal due to another vortex with different V_r and R. As can be seen, the instants of the maxima and minima for the two vortices remain the same.

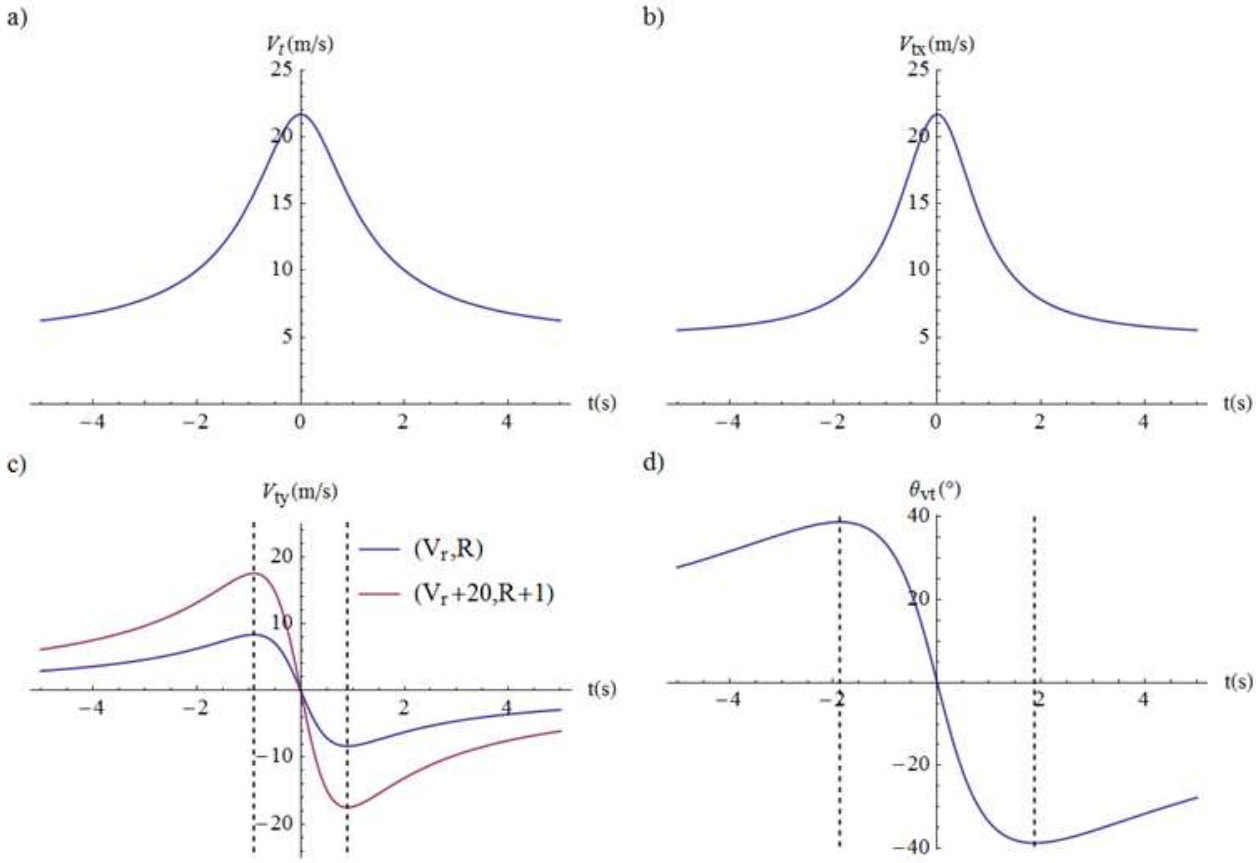

Fig. 5 *Wind speed signatures of a dust devil concordantly rotating as seen by a fixed meteorological station. The event in blue has the following parameters: s = 5 m/s, θ_s = 0, V_r = 25 m/s, R = 3 m, d_o = 4.5 m. The four plots are: a) the total wind speed v_t; b) the x-axis component of v_t; c) the y-axis component of v_t; d) the direction of v_t. In c) and d) the dashed lines indicate the position of the maximum and of the minimum. In c) the dust devils in red has a radius and a rotatory speed 1 m and 20 m/s greater than the blue one. Notice how the stationary points are still located in the same place (dashed lines).*

1.2.2 Discordant Rotation

We now turn to the case of a discordant rotation. In this case:

$$\theta_{vr} = \theta_d + \frac{\pi}{2} \tag{20}$$

for which the following equality holds:

$$cos\ \theta_{vr} = -cos\ \left(\theta_d + \frac{\pi}{2} - \pi\right) = -cos\ (\theta_d - \theta_{do}) \tag{21}$$

$$sin\,\theta_{vr} = -sin\left(\theta_d + \frac{\pi}{2} - \pi\right) = -sin\,(\theta_d - \theta_{do}) \quad \textbf{(22)}$$

where we have used the fact that $\theta_{do} = \frac{\pi}{2}$. Substituting eqs. (13) and (21) in eq.(9) and eqs. (14) and (22) in eq.(10), we get:

$$\mathrm{v}_{tx}(d) = s - \mathrm{v}_r(d)\,\frac{d_o}{d} \quad \textbf{(23)}$$

$$\mathrm{v}_{ty}(d) = -\mathrm{v}_r(d)\,\sqrt{1 - \left(\frac{d_o}{d}\right)^2} \quad \textbf{(24)}$$

In Fig. 7 we show the trend of $\mathbf{v_t}(t)$, its components and direction for a dust devil with the same charactheristcs of that in Fig. 5 but with discordant rotation. The maximum of $\mathbf{v_t}(t)$ is now smaller than in the case of concordant rotations, due to the fact that now s and $\mathrm{v_r}$ are antiparallel in t_o. In addition to this, V_r is usually larger than s (see e.g. Murphy et al., 2016), hence from eq. (23), v_{tx} tends to decrease for $t \rightarrow t_o$. Fig. 7 b) shows the case of $V_r \gg s$, where v_{tx} became negative.

From eqs. (17) and (24) we see that $\mathrm{v}_{ty}(d)$ has opposite trends for concordant and discordant rotation. Its stationary points have the same values in the two cases, and they are again in $d = \pm\sqrt{2}\,d_o (t = \pm\frac{d_o}{s})$. The critical points of the direction $\theta_{vt}(d)$ for a discordant rotation are in $d = \pm\frac{d_o\sqrt{|2s-w|}}{\sqrt{s}}$ $(t = \pm\frac{d_o\sqrt{|s-w|}}{\sqrt{s^3}})$. Both for $\mathrm{v}_{ty}(d)$ and $\theta_{vt}(t)$, the principal difference compared to the concordant case is that the order of the maximum and minimum are inverted, i.e. now the minimum precedes the maximum (see Fig. 7 c) and d)). As we noted, this particular feature makes very easy to recognize the direction of the rotation: one can infer it simply checking the order of the stationary points.

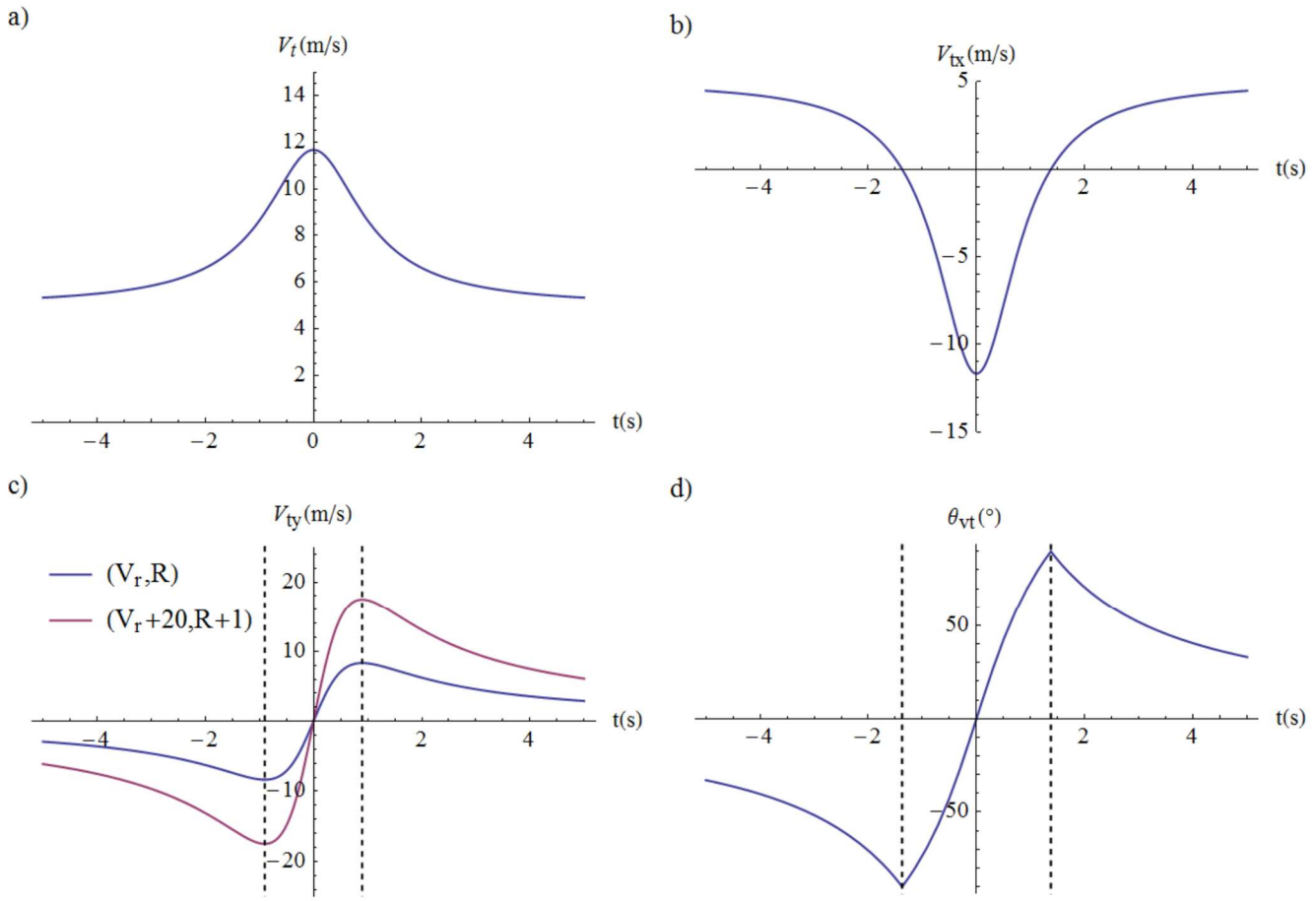

Fig. 6 *Wind speed signatures of a dust devil discordantly rotating as seen by a fixed meteorological station. The event in blue has has the same parameters of the one of Fig. 5: s = 5 m , $\theta_s = 0$, $V_r = 25$ m/s, R = 3 m , $d_o = 4.5$ m . The four plots are: a)the total wind speed v_t; b) the x-axis component of v_t; c) the y-axis component of v_t; d) the direction of v_t. In c) and d) the dashed lines indicate the position of the maximum and of the minimum. In c) the dust devils in red has a radius and a rotatory speed 1 m and 20 m/s greater than the blue one. Notice how the stationary points are still located in the same place.*

Table 2 summarizes the functional form of v_{ty} and the position of its critical points, for both cases of concordant and discordant rotation.

NON-DIRECT PASSAGE	v_{ty} function	Maximum and Minimum position
Concordant rotation	$v_{ty}(d) = V_r \frac{R}{d} \sqrt{1 - \left(\frac{d_o}{d}\right)^2}$	$t = \mp \frac{d_o}{s}$
Discordant rotation	$v_{ty}(d) = -V_r \frac{R}{d} \sqrt{1 - \left(\frac{d_o}{d}\right)^2}$	$t = \pm \frac{d_o}{s}$

Table 2 The impact parameter d_o can be retrieved by studying the component of the measured wind velocity perpendicular to the vortex forward motion (v_{ty}). Indeed, the position of the critical points of v_{ty} is directly related to d_o and s. v_{ty} has simply an opposite behavior in the two cases, hence the only things changing is the chronological order of the maximum and the minimum.

1.2.3 Application of the model

We now turn to the description of the application of the model to the data, in order to find the impact parameter d_o. Even without a priori knowledge of d_o, it is still possible to assess if an event has passed outside or over the meteorological station by some peculiar features of the signals (see e.g. Franzese et al. 2018). The main characteristic of a direct encounter is a double peak trend in the wind speed signal. This is due to the two separate passages over the anemometer of the vortex wall, where the rotational speed has its maximum. Instead, when the passage is not direct, the wind speed signal shows a single peak corresponding to the minimum approach.

The situation most likely to occur is that of a dust devil non-directly passing over the station ($d_o > R$). Recalling paragraphs **Errore. L'origine riferimento non è stata trovata.** and **Errore. L'origine riferimento non è stata trovata.** , we note that the critical points of $\mathrm{v}_{ty}(t)$ for non-direct passage are independent of the direction of rotation and the vortex intrinsic parameter, and that they depend only on d_o and s (see Table 2). In order to evaluate s and its direction θ_s, we consider the data of $\mathrm{v}_t(t)$ and $\theta_{vt}(t)$ relative to a time window of several minutes around the encounter and evaluate their median values to estimate the background wind speed and direction. With the information on θ_b, given the hypothesis $\boldsymbol{s} = \boldsymbol{b}$, we have performed a rotation of the frame of reference to obtain $\theta_s = 0$. In the resulting frame, we have then evaluated $\mathrm{v}_{tx}(t)$and $\mathrm{v}_{ty}(t)$. Lastly, in order to calculate the impact parameter d_o, we have derived the time difference between the maximum and minimum of $\mathrm{v}_{ty}(t)$, obtaining $d_0 = \frac{s\,\Delta t}{2}$.

An alternative derivation can be performed using θ_{vt} instead of v_{ty}. Indeed, it is possible to measure the magnitude of w from the relation $w = \mathrm{v}_t(t_o) \pm s$ (where the ± depends on the sense of rotation, that can be inferred from the trend of $\mathrm{v}_{ty}(t)$ or θ_{vt}). From the critical points of θ_{vt} one gets $\Delta t_\theta = 2\frac{d_o\sqrt{|s \pm w|}}{\sqrt{s^3}}$, hence a relation for d_o is found. Since w is affected by its own uncertainty, this analysis introduces an additional error on d_o.

Considering the low acquisition rate of our survey and the subsequent difficult in the estimation of w, we decided to base our analysis on the study of $v_{ty}(t)$. However, it is important to keep in mind that the analysis of θ_{vt} can be crucial when only the wind direction is available.

The data used for the analysis have been obtained by the anemometer at 3.35 m from the ground. The software to analyze such data has been developed in C programming language, and it is available upon request.

1.2.4 Reconstruction of the vortex intrinsic parameters

By knowing the impact parameters d_o of the dust devils encounters, it is possible to easily estimate the intrinsic vortex wind speed and pressure drop. Indeed, using the measured pressure drop $\Delta P(t)$ signature and the value of d_o we can directly retrieve the value of the intrinsic drop ΔP_o (eq.(2)).

We can then couple the equation of the cyclostrophic balance eq.(3), and the equation of Rankine vortex rotation model eq.(1) to obtain a system in the variables V_r and R. For example, in the case of not direct passage, evaluating the eq.(1) in d_o, we obtain:

$$\begin{cases} \frac{\Delta P_o}{\bar{P}}\bar{T} = \frac{V_r^2}{R} \\ v_r(d_o) = V_r\frac{R}{d_o} \end{cases} \quad \textbf{(25)}$$

$v_r(d_o)$ is the quantity we defined as w and is measurable from the acquired signal, while with the other meteorological measurements we can evaluate the environmental temperature $\bar{T}$ and pressure $\bar{P}$. Therefore, we can resolve the system to calculate the intrinsic rotatory speed V_r and the radius R of the dust devil.

Another easy measurable quantity related to the rotatory speed is the value that v_y assumes in the stationary points:

$$v_y\left(\sqrt{2}d_o\right) = \frac{1}{2}V_r\frac{R}{d_o} \quad \textbf{(26)}$$

this quantity can be used in eq.(25) in place of $v_r(d_o)$, obtaining an equivalent system.

Depending on the specific characteristic of the survey, other equivalent combinations of observable quantities can be used, but overall, once the impact parameter is known, the size/distance degeneracy expires and it is possible to combine the acquired pressure and wind speed signatures to evaluate the whole set of vortex intrinsic characteristics ΔP_o, V_r and R.

1.3 Image processing

In order to validate our technique, we compared the impact parameters estimated through the model with the ones we obtained by the acquired images. Here, we briefly describe the method we used to analyze the images, that we developed in the Wolfram Mathematica® environment.

The collected images represent the 2D projection of our site as seen by our camera. This projection is not isometric, i.e. it does not preserve the measurable quantities (angles and lengths). In order to reconstruct distances, we need to remap the images on an isometric frame, that we have chosen to be the bird's-flight view of our site (i.e. the view-plan in isometric projection). We called *Oxy* the system of orthogonal coordinates on this isometric plane and, in order to refer all the distances directly to the station, we placed the center on it.

As shown in Fig. 7, we have outlined on the ground around the station 1 full circle and 4 arcs of different radii (specifically, 3, 6, 9, 12 and 18 m). In addition to that, we have positioned 3 sets of stones at 21, 27 and 34 m from the station. We will use these marks as reference for finding the relative distances.

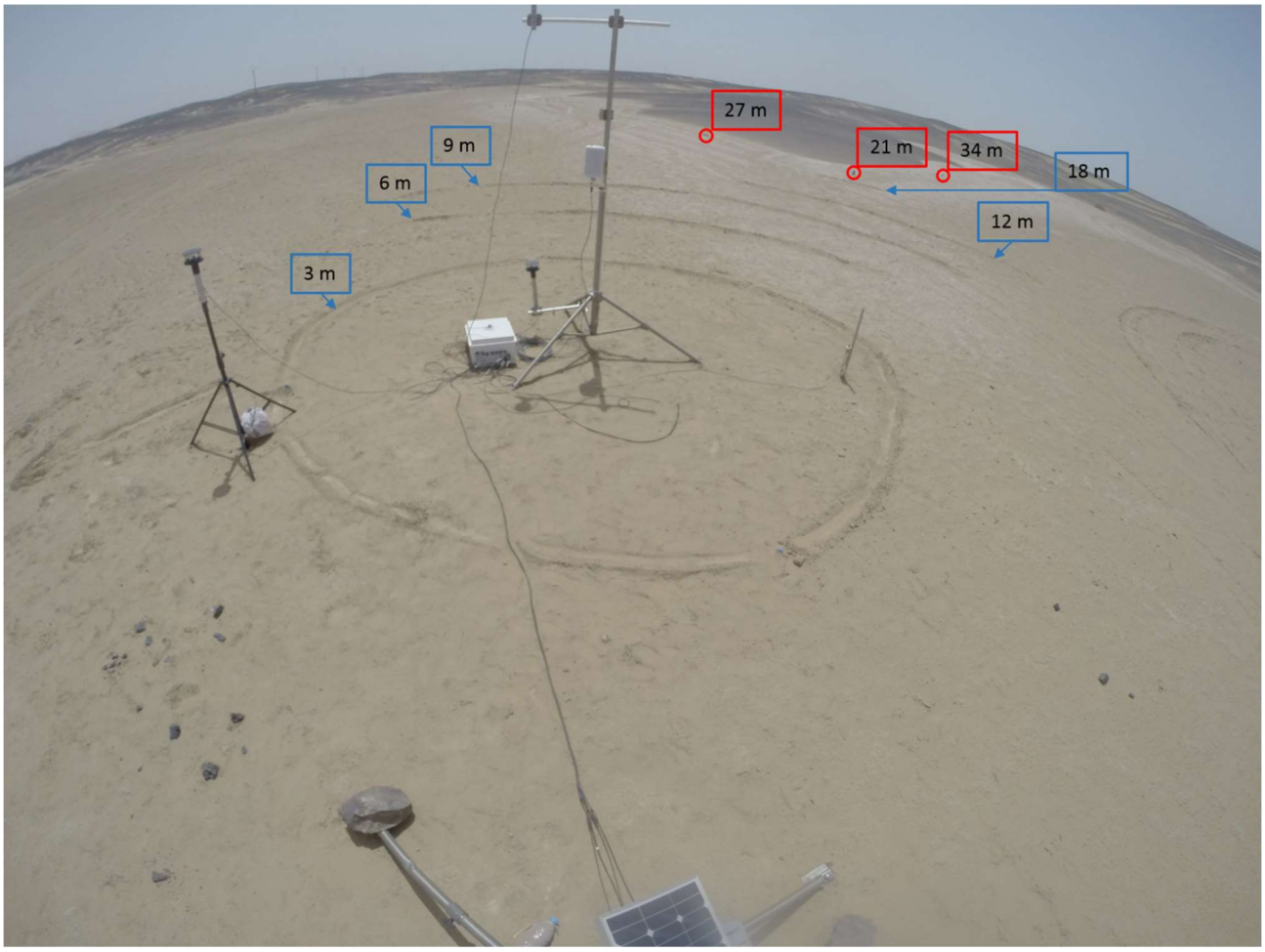

Fig. 7 ***An image acquired by our mounted camera, where are visible the marked arches (in blue, at different distances) and rocks (in red) that we used to reconstruct the distances.***

To process the images, we need to correct for the fish-eye effect (visible in *Fig. 7*) that arises from the grand angle lens of the camera (the details of the correction are not outlined in this paper). Once this effect is removed, we have defined on the corrected image a system of coordinates *O'x'y'*. For convenience, it is centered on the lower left corner of the image, as indicated in Fig. 8.

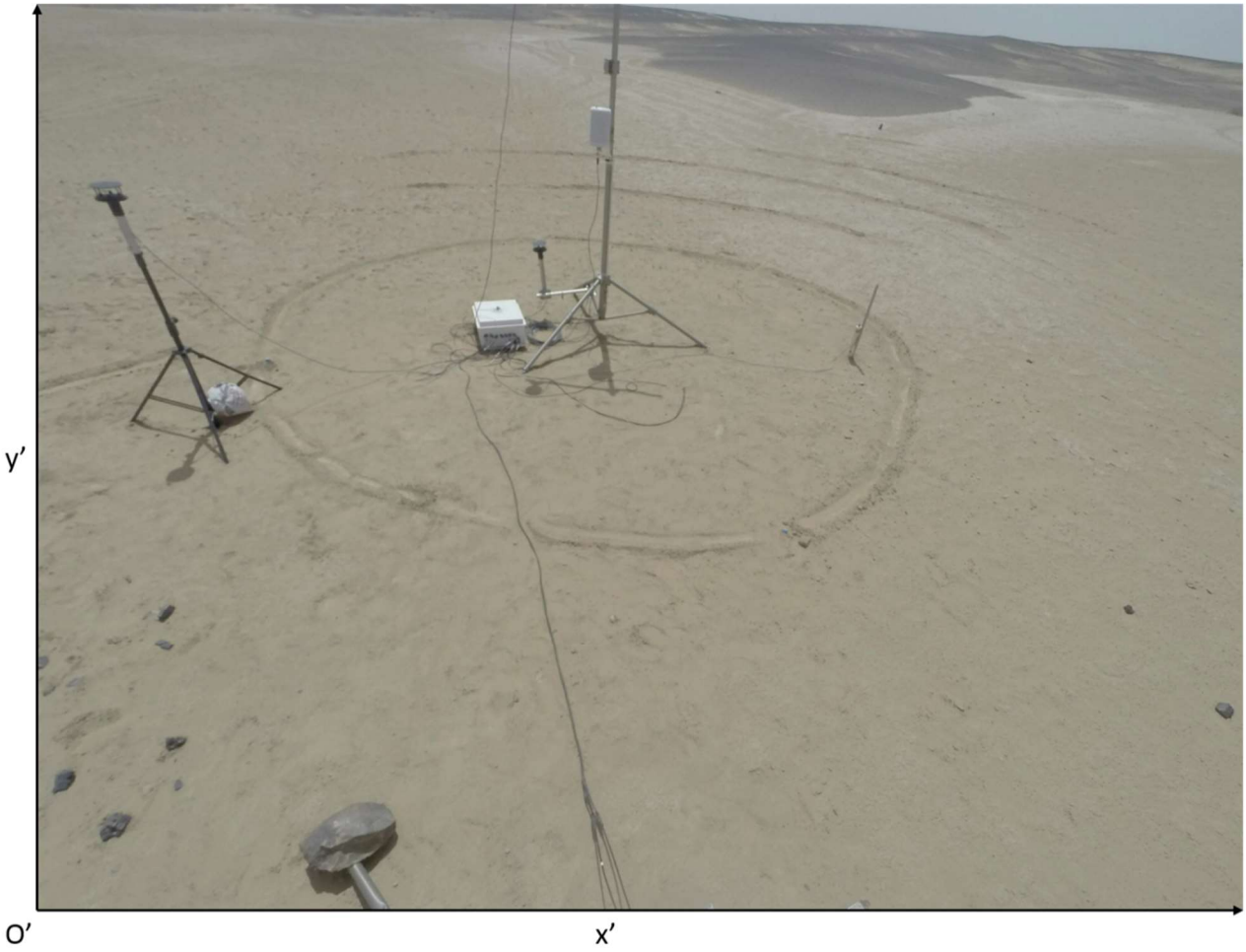

406

407 **Fig. 8 Correction of *Fig. 7* after accounting for the fish-eye effect. Note also the definition of the frame of reference *O'x'y'*.**

408

409 The range of the x' and y' axes are known due to the fixed size of the images, which are set at
410 1024x768 pixels. Hence:

411 $$x' \in [0, 1024] \qquad y' \in [0, 768]$$

412 In order to perform the O*xy*→*O'x'y'* mapping, we need to derive the parameters of the transformation
413 matrix. Due to its nature of superposition of rotation, translation, skew and scaling, we are interested
414 in a 9-parameter bilinear mapping, also known as Möbius transformation. Restricting our analysis to
415 the 2D case, we get a matrix of the form:

$$M = \left(\begin{array}{cc|c} a_{11} & a_{12} & b_1 \\ a_{21} & a_{22} & b_2 \\ \hline c_1 & c_2 & d \end{array}\right) \tag{27}$$

416 from which it follows:

$$\begin{cases} x' = T_x(x,y) = \dfrac{a_{11}\,x + a_{12}\,y + b_1}{c_1\,x + c_2\,y + d} \\ y' = T_y(x,y) = \dfrac{a_{22}\,y + a_{21}\,x + b_2}{c_1\,x + c_2\,y + d} \end{cases} \quad \textbf{(28)}$$

where we have used the notation T(x,y) to indicate the transformation and (a_{ij}, b_i, c_i, d) its parameters. We outline the description of the methodology followed to derive the parameters in the following section.

1.3.1 Fitting procedure

Let us call D_M the distance of each mark from the station, $D_M = \sqrt{x_M^2 + y_M^2}$. Using the inverse map T^{-1}, this expression in *O'x'y'* can be written as:

$$D_M = \sqrt{T_x^{-1}(x'_M, y'_M)^2 + T_y^{-1}(x'_M, y'_M)^2} \equiv \quad \textbf{(29)}$$

$$\equiv \sqrt{\frac{(a_{21}b_1 - a_{11}b_2 + (b_2c_1 - a_{21}d)x' + (-b_1c_1 + a_{11}d)y')^2 + (-a_{22}b_1 + a_{12}b_2 + (-b_2c_2 + a_{22}d)x' + (b_1c_2 - a_{12}d)y')^2}{(-a_{12}a_{21} + a_{11}a_{22} + (-a_{22}c_1 + a_{21}c_2)x' + (a_{12}c_1 - a_{11}c_2)y')^2}}$$

We performed a 9 parameters fit of function of eq. (29) using the whole set of marked points. The algorithm chosen for the least-square estimation is the Levenberg-Marquardt (Levenberg, 1944; Marquardt, 1963), with starting point the set of parameters $({a_{ij}}^V, {b_i}^V, {c_i}^V, d^V)$ derived in Appendix-B. Note also that we have relaxed the additional constraint on the scaling used for the decision of the starting fitting point.

Fig. 9 shows our best fit model ($R^2 = 0.9994$), the agreement of the map with the frame is clearly evident.

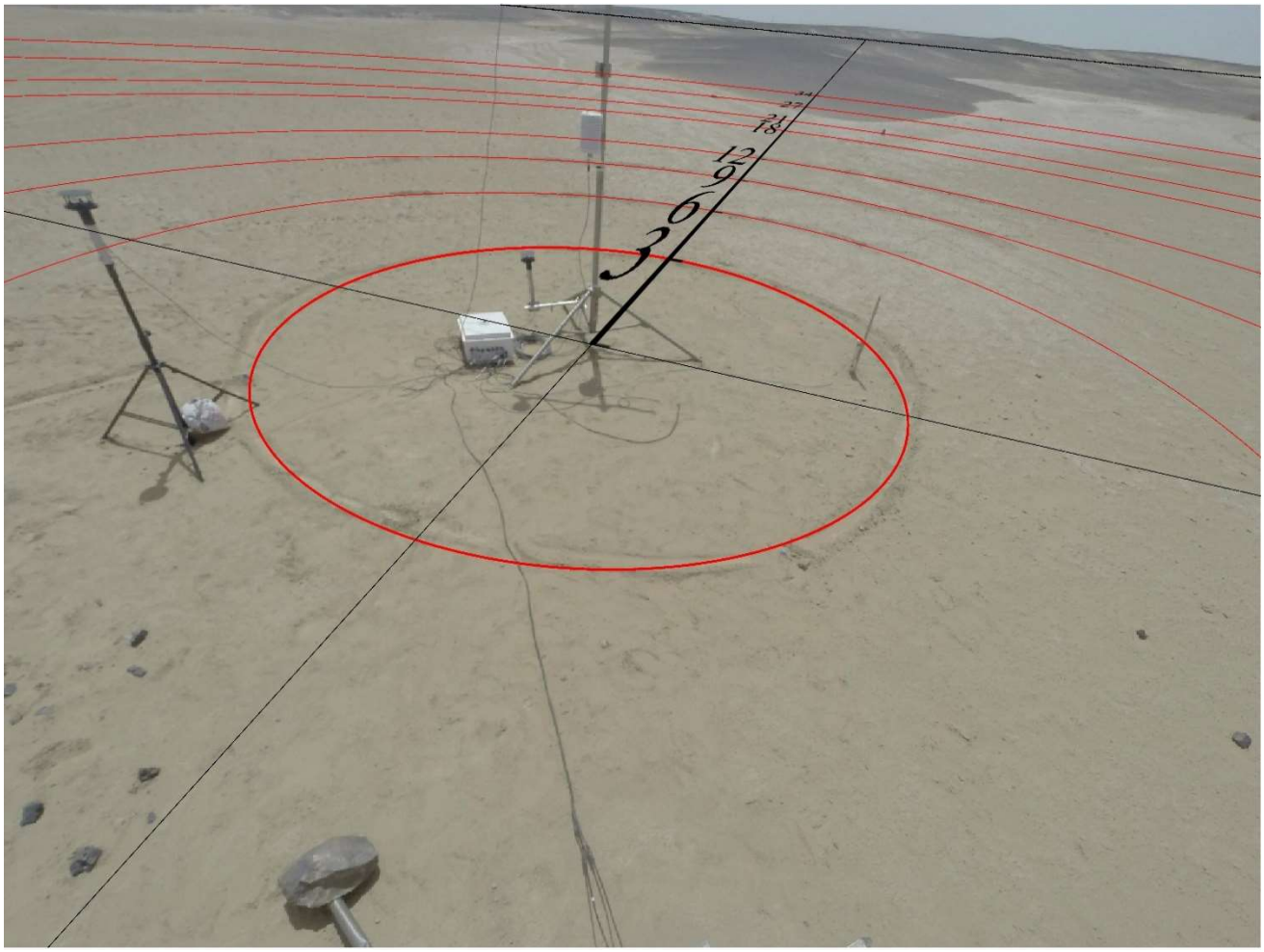

Fig. 9 *The result of our mapping of the horizontal plane on the images taken by the mounted camera. In red we plotted the circles passing for each marked points (radius of 3,6,9,12,18,21,27 and 34 meters as shown). In black we plotted the axes x and y relative to the original system of coordinates Oxy and the evaluated horizon line. Each marked point and the horizon are well fitted from this map.*

In order to ensure that the results of the fit remain consistent, we have varied the starting point. Fig. 10 shows two of such results. As it can be seen, the set of curves coincide, and the distances resulting from the different starting points are consistent well within errors in all our tests. It is worth highlighting that this procedure returnes distances, e.g. the direction of the axis is not fix. This allows in principle to find all the possible frames of reference that can be obtained by rotation of our solution.

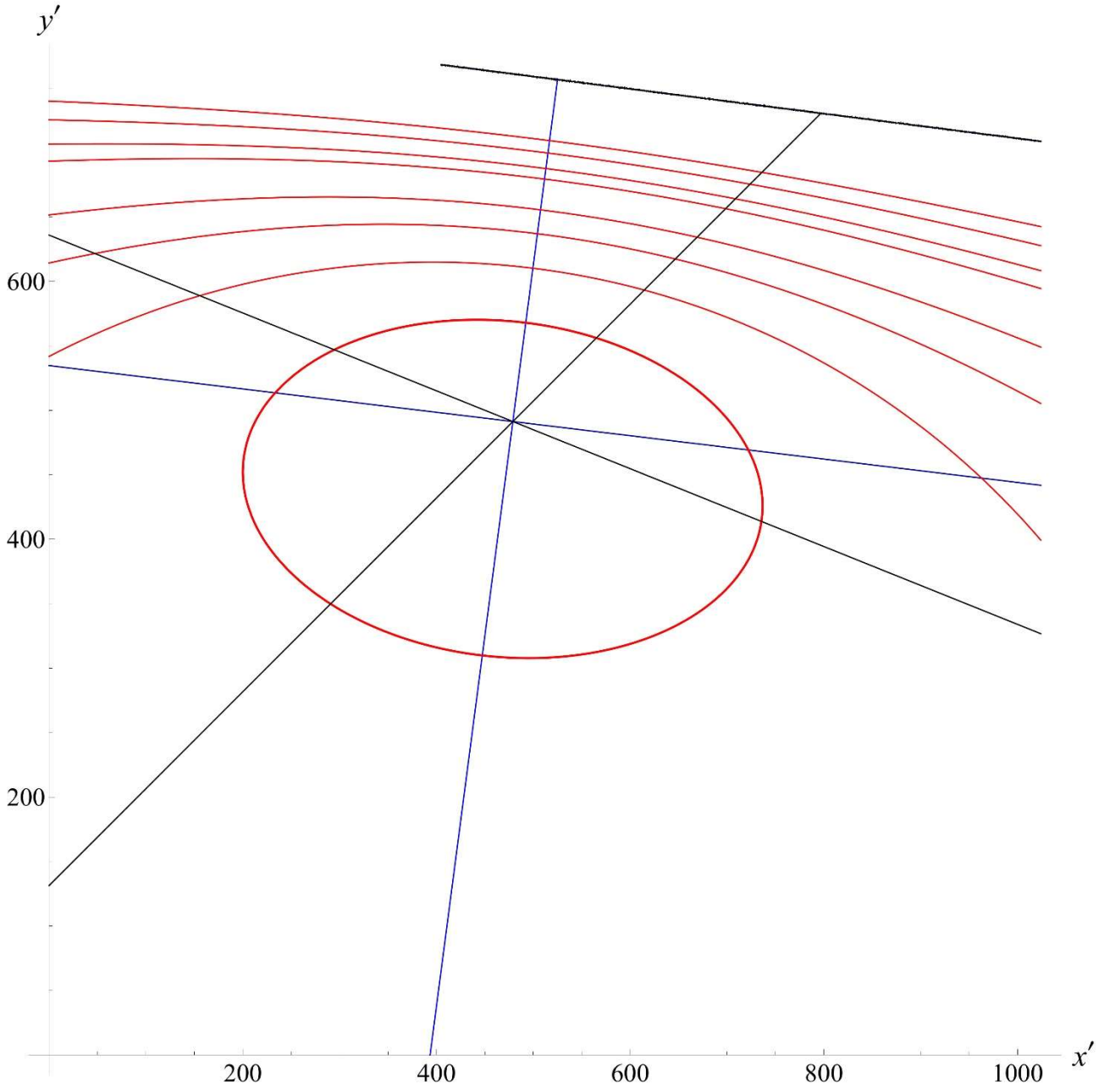

Fig. 10 *Two results of the map fitting obtained using two different set of initial parameters values. The axis of the two systems obtained are plotted in black and blue, while we plotted in both cases the circles of radius 3,6,9,12,18,21,27,34 meter in red. The result coincides, as the horizon lines.*

Once the transformation parameters are known, the determination of the distances d proceeds as follows. The position (x'_D, y'_D) in *O'x'y'* of the vortices can be measured directly from the images, as described in the next paragraph. We can then apply *T(x,y)* to get the coordinates of the dust devil in *Oxy* by mean of:$x_D = T_x^{-1}(x'_D, y'_D)$ and $y_D = T_y^{-1}(x'_D, y'_D)$. d will hence be: $d = x_D^2 + y_D^2$.

1.4 Selection of the events and individuation of their position

We performed the selection of the dust devils events recorded by our instruments by checking directly the acquired images. Due to the low contrast between the dust devil and the background composed of sky and sand, we have arranged an initial phase aimed to determine the most suitable region of image for the dust devil recognition. After thorough selection of the camera height and angle, we have chosen such background to be the black area visible in Fig. 3, which is composed of low hills covered by dark pebbles. The events that we were able to easily identify are concentrated in the last two days of the measurement process.

Once the passage of the dust devil has been recognized, we processed the relative images in order to make clear its position in the pictures. In particular, we use a process of image subtraction between the ones where the vortex is visible and one taken just before its appearance, in order to isolate the differences and highlight the vortex.

2. Results

We focused on the last two days of measurement, where we acquired a data set of nine events suitable to be analyzed with both techniques. Fig. 11 shows the image of the closest approach of one of the vortices observed on 23 July, the whole sequence of its passage is shown in Fig. 12.

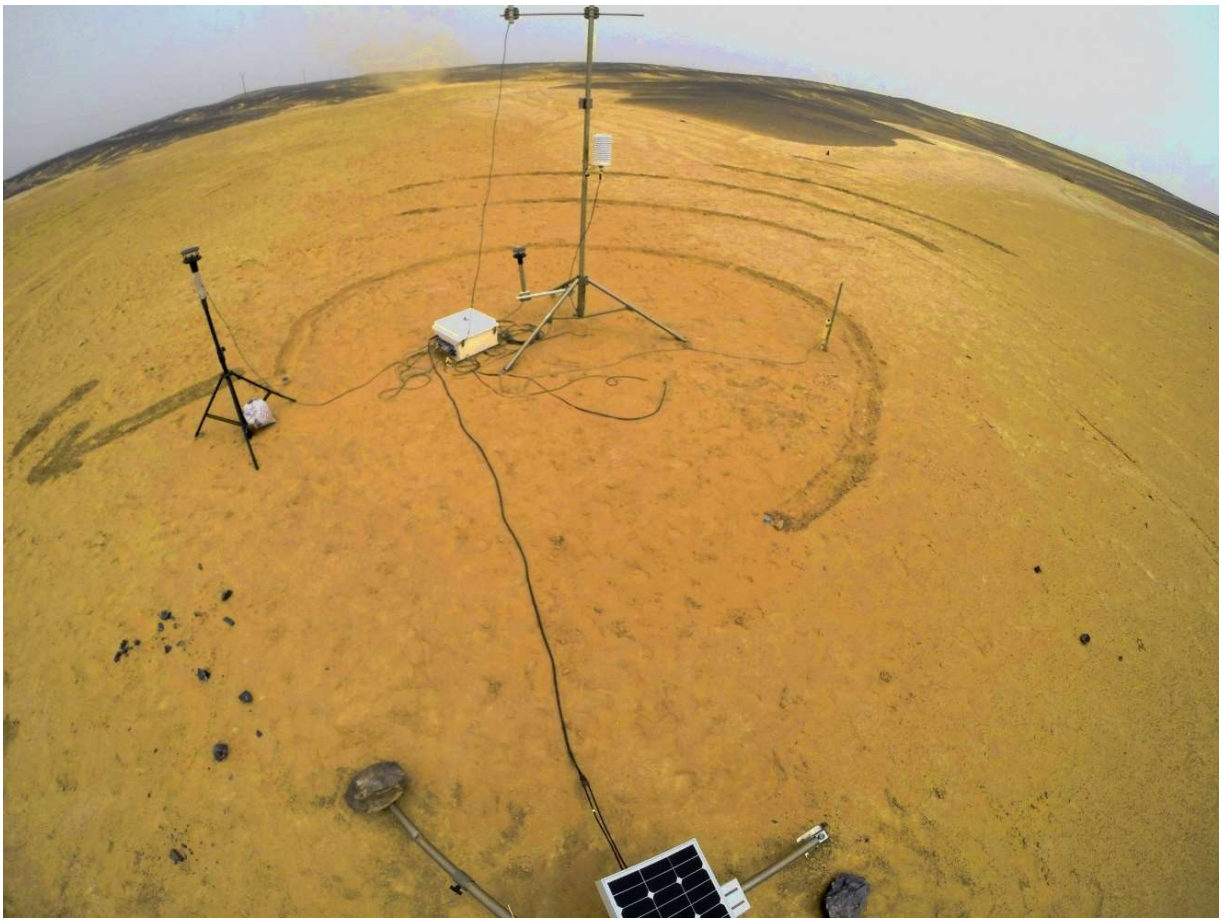

Fig. 11 *The passage of a dust devil caught by our camera at July 23 around 3 p.m.. The vortex is particularly clear against the black hills background; the colors have been stretched to make it visible also against the sky background.*

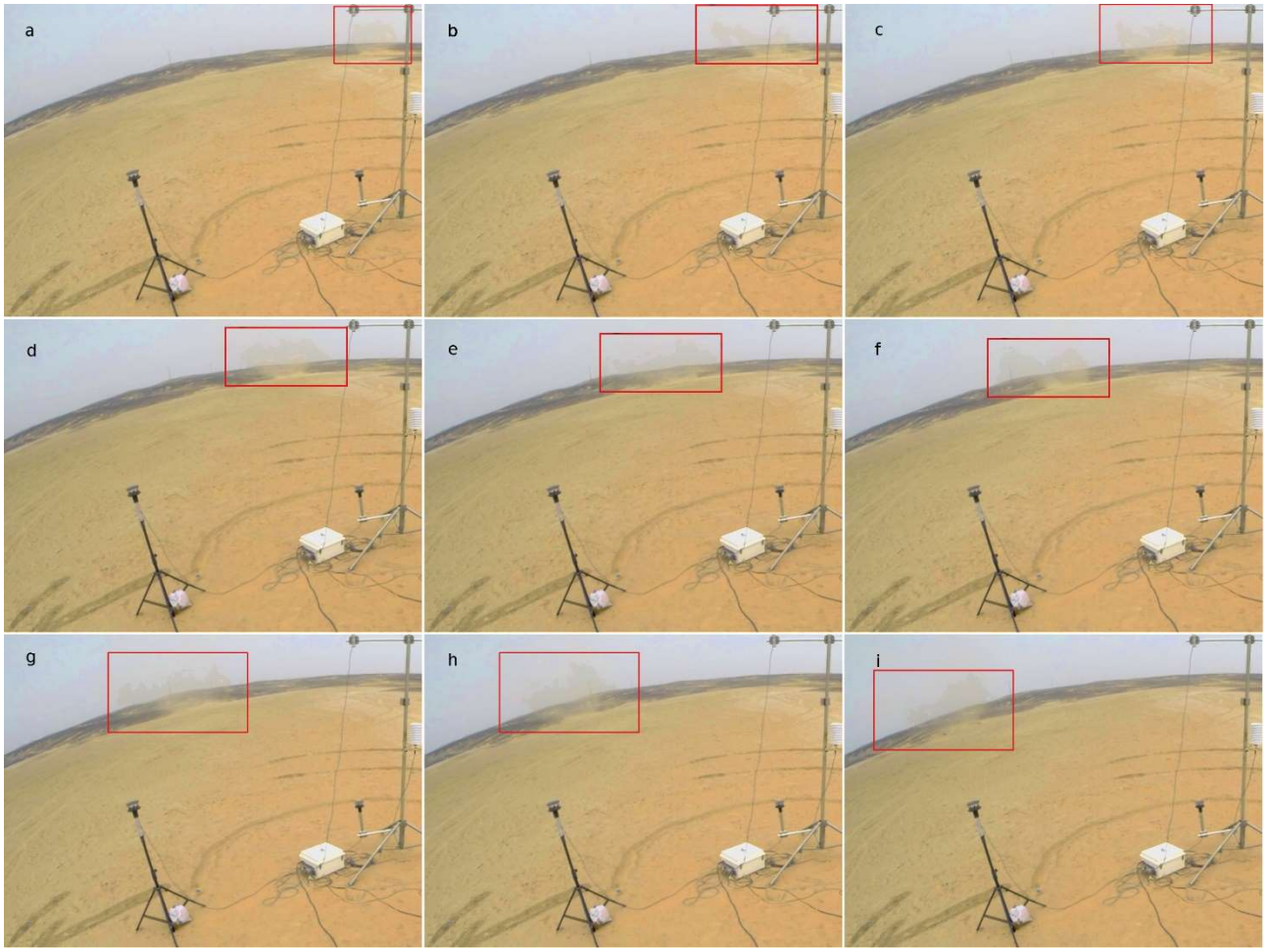

Fig. 12 The dust devil of Fig. 11 during its passage at ~ 61 m from the station.

Fig. 13 shows the same sequence after the image processing procedure described in par. 1.4.

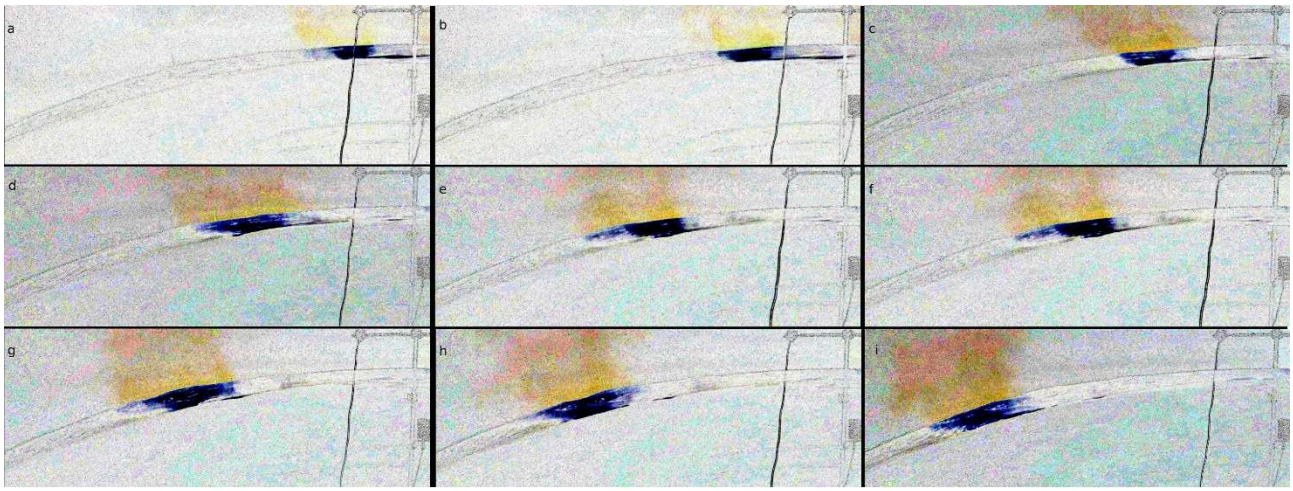

Fig. 13 The dust devil sequence of Fig. 12 after the image subtraction process used to isolate the presence of the vortex.

We observed both sense of rotation in our sample, e.g. Fig. 14 and Fig. 15 show the wind speed and direction signature for two of the vortex encounters. The first event rotates concordantly, as can be notice from the θ_{vt} and v_y trends (Fig. 14 b and d: the maximum precedes the minimum). In this case, we expect that the vortex velocity follows the trend shown in Fig. 5. In particular, the x-projection of the velocity and the total wind speed have to reach the same magnitude (eq. (18)), how can be seen from the data (Fig. 14 a and c). The event depicted in Fig. 15 rotates discordantly: in plots b and d, the minimum precedes the maximum. The x-components of the translational speed s and rotational speed v_r are opposite in d_o (see eq. (23) and Fig. 6). If the measured v_r has a magnitude comparable to s, the component v_x of the velocity can results completely covert. This is the case of Fig. 15, where both v_r and s reach a magnitude around 4 m/s and the signature of the vortex passage is not visible in v_x (plot c).

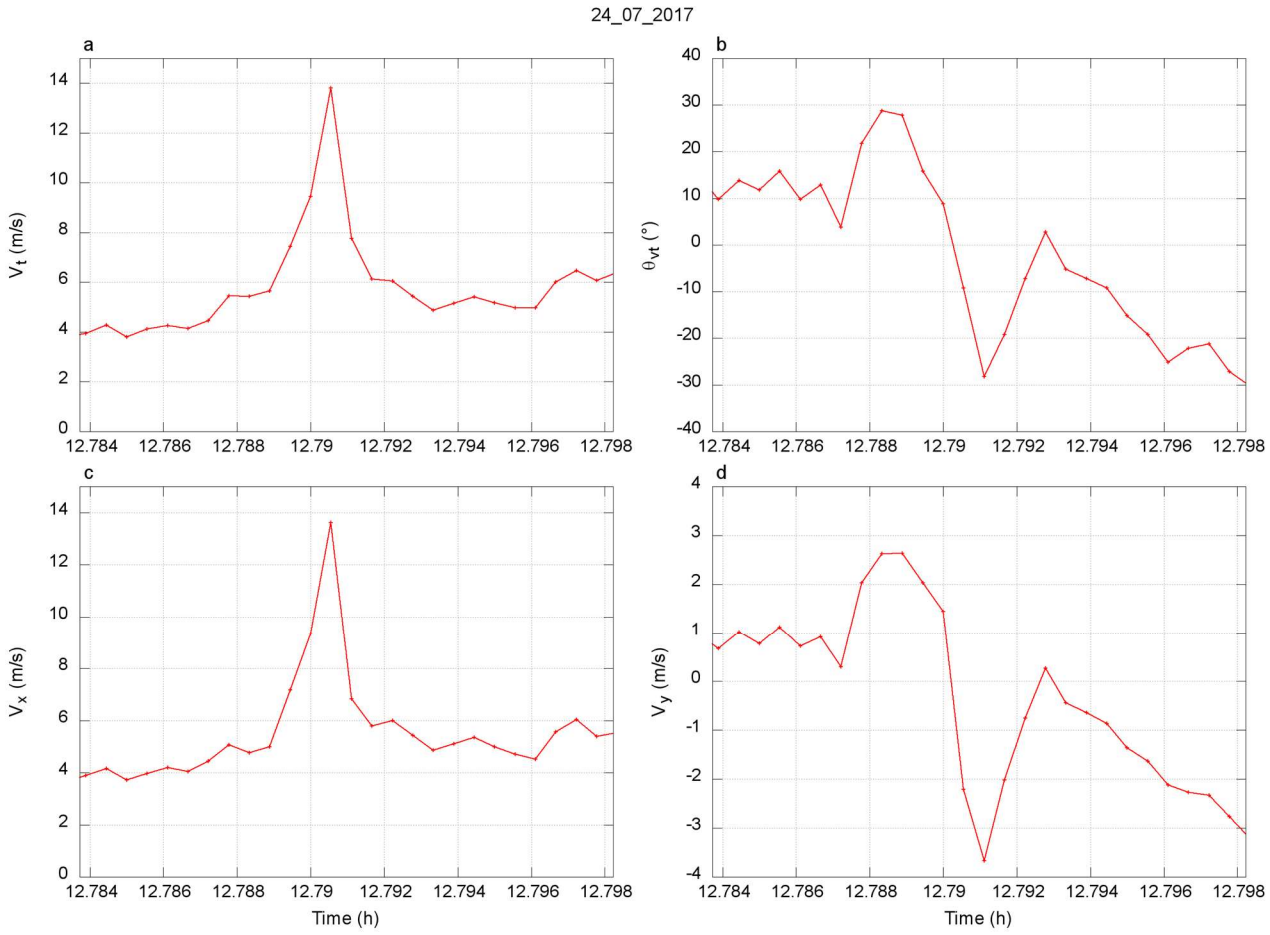

Fig. 14 The wind speed and direction signature of one of the passing dust devil. a) shows the total wind speed v_t (the direct measure of the anemometer); b) the direction of the vector v_t already normalized to zero mean; c) the x-projection of v_t (where

x is the direction of the translational motion of the vortex); d) the y-projection of v_t. In the b and d plots the maximum of the signature precedes the minimum and this indicates that the vortex rotates concordantly to its translational motion.

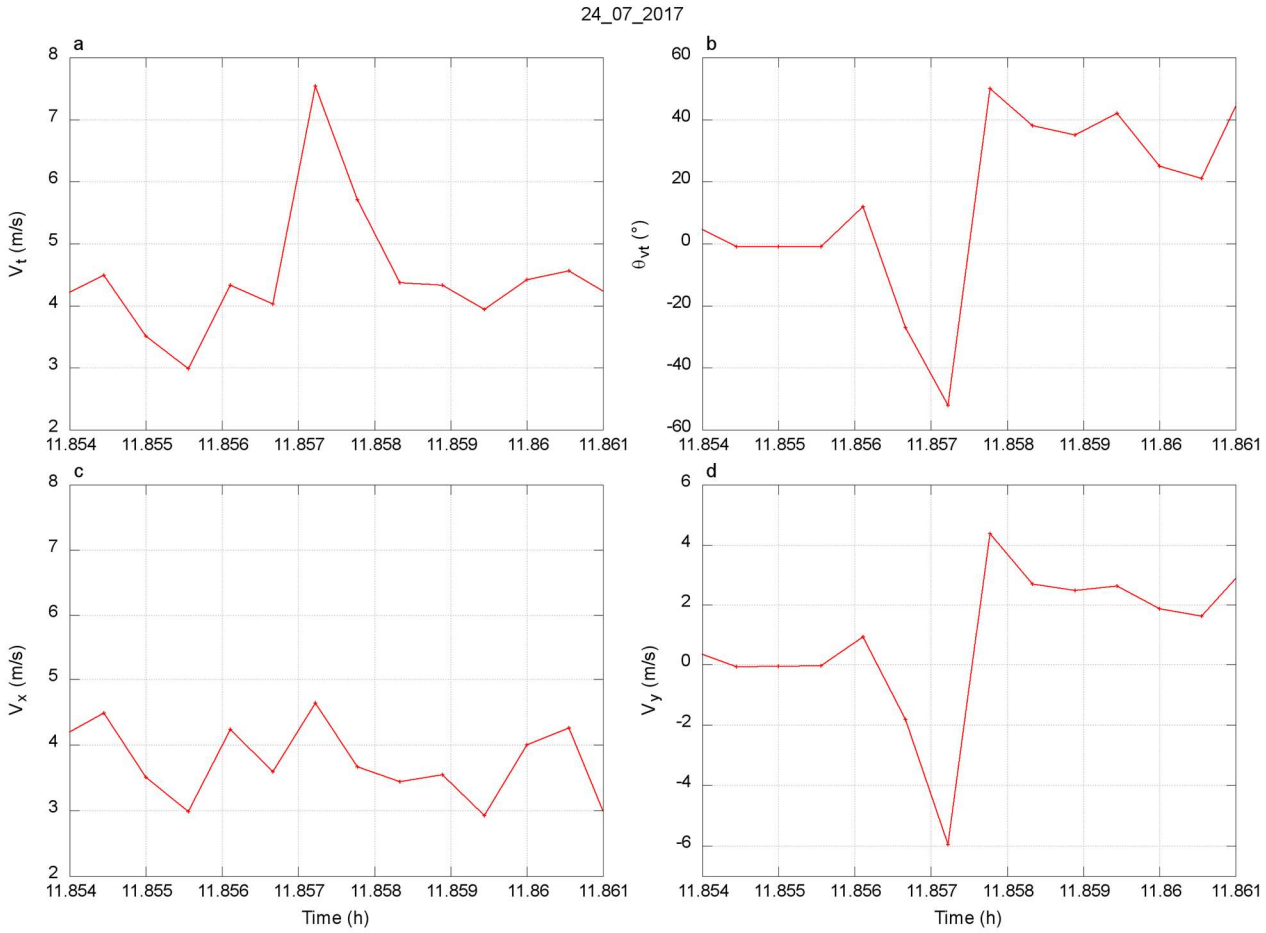

Fig. 15 The wind speed and direction signature of one of the passing dust devil. Fig. a) shows the total wind speed v_t (the direct measure of the anemometer); b) the direction of the vector v_t already normalized to zero mean; c) the x-projection of v_t (where x is the direction of the translational motion of the vortex); d) the y-projection of v_t. In the b and d plots the minimum of the signature precedes the maximum and this indicates that the vortex rotates discordantly to its translational motion.

The observed distances range from few meters to more than 100 meters. The rate of acquisition is 2 Hz, hence the main source of uncertainty is the distance between the positions of the dust devil between two consecutive measurements. Therefore, we have estimated the uncertain level using the measured value of s (the vortex travelling speed). The uncertain is doubled on the wind signal analysis, because we have to evaluate both the maximum and minimum positions of the curve.

Table 3 reports the obtained results for the whole dust devils set.

date	t_i	$d_{o\ wind}$	$d_{o\ images}$
23_07_2017	12.78	15 ± 8	13 ± 4
23_07_2017	13.76	53 ± 10	57 ± 5
23_07_2017	14.67	54 ± 8	47 ± 4
23_07_2017	14.72	56 ± 8	62 ± 4
24_07_2017	10.38	30 ± 10	29 ± 5
24_07_2017	10.545	50 ± 10	45 ± 5
24_07_2017	11.145	43 ± 10	46 ± 5
24_07_2017	11.3	156 ± 10	149 ± 5
24_07_2017	11.857	4 ± 8	3 ± 4

511 **Table 3** ***The impact parameters d_o obtained from the wind signal analysis ($d_{o\ wind}$) and from the images ($d_{o\ images}$). t_i is the initial***
512 ***time of the event in hour fraction***

513

514 Fig. 16 shows the comparison of the different results. All the points lie on the bisector, within the
515 errors.

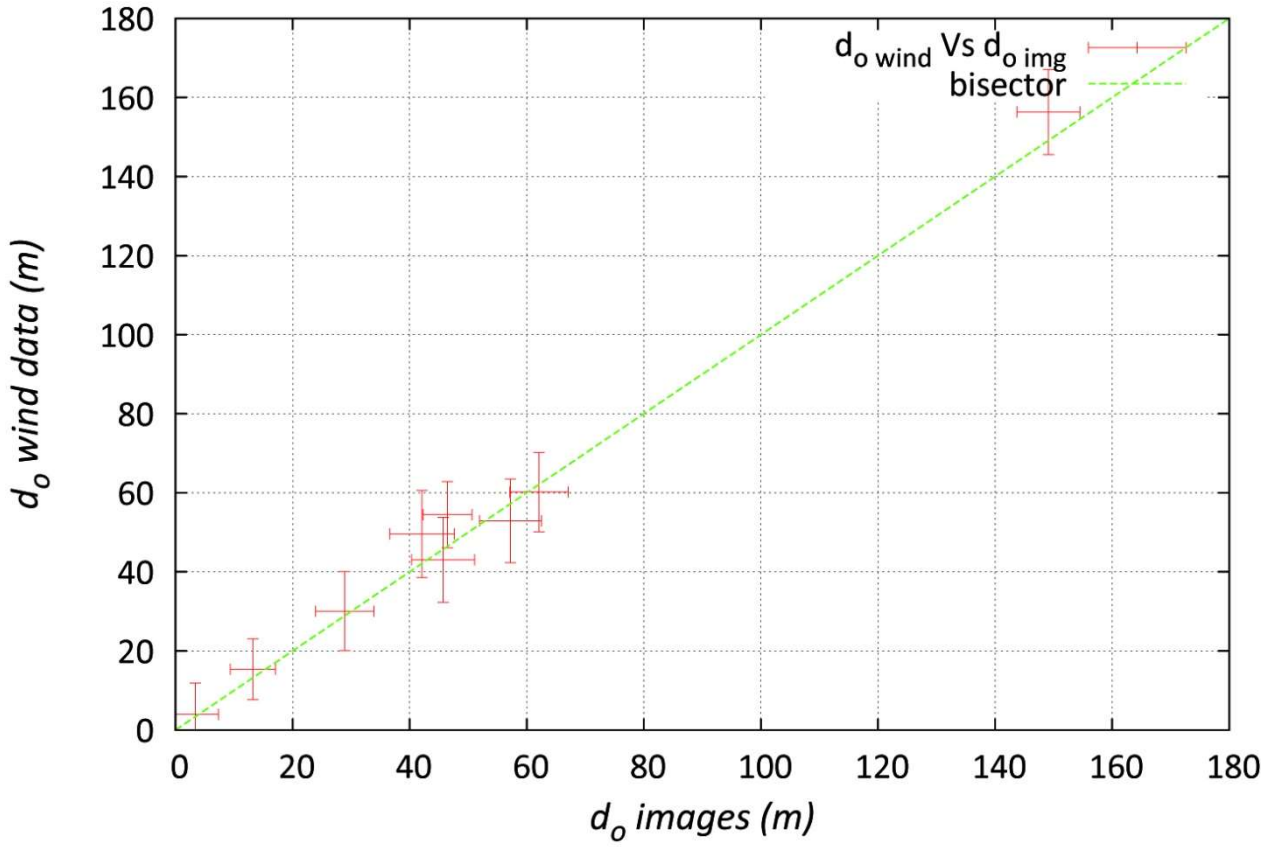

Fig. 16 *The impact parameters d_o obtained from the images on x axis, compared with the ones obtained by the study of the wind speed signal. All points are compatible within uncertainties with the bisector, proving the agreement of the two methods.*

3. Discussion

Lorenz, 2016 has proposed a heuristic procedure to retrieve simultaneously the intrinsic vortex characteristics (V_r, ΔP_o, R) and the geometrical parameters of the encounter (s, ϑ_s, d_o) by fitting the acquired pressure, wind speed and direction time series. Overall, the process involves the use of six parameters that decrease to four in the restricted model, where the traverse speed and direction of the vortex are imposed equals to the environmental values, an analogue approach to the one used in this paper. The model is able to achieve good fits of the dust devils signals. However, it is not able to fully resolve the size/distance degeneracy because the fit result is not unique. The vortex sense of rotation has to be supposed a-priori, hence the analysis has to be repeated supposing both sense of rotation. Moreover, the obtained best fit can heavily depends on the chosen starting value of the fit parameters. There are cases where different set of the parameters (V_r, ΔP_o, R, d_o) can fit sensibly better one of the

three time-series (pressure, wind speed and wind direction) than the others, leading to an ambiguity in the choice of the more significant result.

The method we propose does not involve a simultaneous analysis of all the intrinsic and geometric parameters. We study the wind data to find the impact parameter and sense of rotation of the events. The evaluation of these quantities arises from the study of the signal trend and does not allow any ambiguities. With the analysis of the pressure data, it is possible to obtain the intrinsic vortex parameters as the pressure core drop, the wall rotatory speed and the vortex diameter.

Theoretically, this procedure does not require any fitting. The only requirement is the solution of a series of equations proper of the model. In the case of the real data, it could be impossible to determine directly the position of the stationary points, due to instrumental limitation and non-uniformity of the wind background. In this case, a fitting procedure can be implemented to improve the technique. However, the current work is aimed to test our model, hence we decided to leave the procedure as straightforward as possible.

One of the main issues we faced during this study has been the difficulty to collect a sufficient number of vortices suitable for our test. The event has to pass inside the visual cone of the camera, in a portion of the image where there is enough contrast to be recognizable, and have to remain visible until it reaches the minimum distance d_o from the station. In addition, the meteorological signatures have to clearly show the distinctive change in wind direction proper of the vortex rotation. In some cases, dust devils recognizable in the pictures did not leave a suitable track in the wind data. This is related to the quality of the acquired signal: a high noise level due to a high wind turbulence or a too low acquisition rate can mask the trend of θ_{vt} and v_y preventing the individuation of the stationary points, in particular for the small vortices that pass far from the station.

The main purpose of the technique described here is, however, to analyze the meteorological signatures that are already clearly recognizable as dust devils, without the use of an additional camera. It is not intended to be used to clarify doubtful signals. The issues we faced are proper of the test performed to validate the technique and not of the technique itself.

556 The low acquisition rate and the short campaign length have also prevented the test of the applicability
557 of the model to the case of dust devils passing over the station. This eventuality is indeed quite rare
558 and even if we have observed an event with a d_o compatible with 0, the vortex would have passed too
559 fast relatively to our acquisition rate to catch the double peak trend of the signal v_t. However,
560 considering that the case of a direct passage already puts strong constrains on the possible impact
561 parameter of the encounter, the ability to study the distance of passage for the not direct passages,
562 where we have no information at all on d_o, is overall more useful in most surveys.
563 As we mentioned, the limits of applicability of the model heavily depends on the signal to noise ratio
564 that rapidly decreases with the event distance. However, our method has proven to be suitable even
565 for dust devils with quite high impact parameter, indeed the farthest vortex has been measured at 150
566 m from the station.

567 ## 4. Conclusion

568 We presented the analysis of two days of dust devils activity acquired during a field campaign in the
569 Sahara desert in Morocco. We monitored the whirlwinds using a meteorological station equipped
570 with a single grand-angle camera. The purpose of this work is the validation of a simple model, based
571 on the Rankine vortex model, to find the geometrical parameters of the encounters using the acquired
572 wind speed and direction time series, in particular the distance of passage of the vortex from the
573 station (impact parameter) and its sense of rotation. The impact parameters evaluated with the camera
574 images of the events have been used to test the model.
575 The technique requires only the monitoring of the wind and it is therefore applicable to every dust
576 devil survey that includes an anemometer. When coupled with the measurement of the pressure time
577 series of the events, our model allows also to directly derive the pressure core drop, the wall rotatory
578 speed and the radius of the vortex, thus enabling the complete characterization of the event.
579 The test of the technique has given good results, showing as all the distances estimated using the
580 model are compatible with the ones from the images.

581 The ability to add the information on the vortices passage distance with its meteorological and
582 morphological parameters greatly enhances our possibilities to study the physics of dust devils.
583 Indeed, the results obtained so far are affected by a size/distance degeneracy that greatly limits the
584 capacity to study individually the different vortex parameters and the correlations among them.
585 For example, we do not know how the electromagnetic, seismic and dust concentration signatures
586 depend on the distance and on the vortex size.
587 In particular: (CHE C'ENTRA CON IL FATTO CHE NON SAPPIAMO COME LE PROPRIETA@
588 ELETTRICHE ECC DIPENDONO DALLA DISTANZA?)
589 - the ESA/Roscosmos ExoMars 2020 mission will host on its lander also a meteorological
590 station (METEO package) and the Dust Complex: a specific suite of instruments for the study
591 of the airborne dust, comprehensive also of an atmospheric electric sensor, an electromagnetic
592 activity probe (EMA) and an optical particle counter for the dust concentration and size
593 distribution characterization (MicroMED);
594 - and the NASA InSight 2018 hosts a seismometer and magnetometer in addition to the pressure
595 and anemometer sensors (Spiga et al., 2018).
596 The procedure we proposed is useful not only in the frame of the next missions. It can be used to
597 improve the analysis of the previous surveys, both terrestrial and martian. In particular, the authors
598 foreseen a new study of the data published in Franzese et al. 2018, to analyze how the vortex induced
599 electric field depends on the distance, pressure, rotational speed and lifted dust concentration.
600

601 # APPENDIX – A

602 ## Dust Devils direct passage case

603

Here we an application of the model for direct passage of the dust devil over the instruments. As in the case of non-direct passage, we study separately the two geometries of concordant and discordant rotation.

A.1 Concordant Rotation

The overlap between the dust devil and the meteorological station happens for $|d| \leq R$, during the time interval $t \in [-\frac{\sqrt{R^2-{d_o}^2}}{s}, +\frac{\sqrt{R^2-{d_o}^2}}{s}]$. Using eqs.(1b), (16), (17) for this time range we get:

$$\mathrm{v}_{tx}(d) = s + V_r \frac{d_o}{R} \tag{30}$$

$$\mathrm{v}_{ty}(d) = V_r \frac{d}{R} \sqrt{1 - \left(\frac{d_o}{d}\right)^2} \tag{31}$$

Fig. 17 shows the trend of $\mathrm{v}_t(t)$, $\mathrm{v}_{tx}(t), \mathrm{v}_{ty}(t)$ and $\theta_{vt}(d)$ for a dust devil with the same intrinsic parameter of that of Fig. 5 and passing at $d_o = 1\,m$ from the station. The resulting total velocity $\mathrm{v}_t(d)$ has a different behavior from the case of non-direct passage: it has one peak in $d = d_o$ ($t = t_o$), and two additional peaks at $d = \pm R$ ($t = \pm\frac{\sqrt{R^2-{d_o}^2}}{s}$), see Fig. 17 a. Note that v_{tx} (eq.(30)) does not depend on *d*, and hence it is constant during the entire duration of the passage over the station (Fig. 17 b). On the other hand, v_{ty} has maximum and minimum for $d = \pm\sqrt{2}\,d_o$ ($t = \pm\frac{d_o}{s}$) when $R < \sqrt{2}d_o$, and for $d = \pm R$ ($t = \pm\frac{\sqrt{R^2-{d_o}^2}}{s}$) when $R > \sqrt{2}d_o$ (Fig. 17 c). $\theta_{vt}(d)$, the direction of $\mathrm{v}_t(d)$, has stationary points in $d = \pm\frac{d_o\sqrt{2s+w}}{\sqrt{s}}$ ($t = \pm\frac{d_o\sqrt{s+w}}{s}$) for $R < \frac{d_o\sqrt{2s+w}}{\sqrt{s}}$, and in $d = \pm R$ ($t = \pm\frac{\sqrt{R^2-{d_o}^2}}{s}$) for $R > \frac{d_o\sqrt{2s+w}}{\sqrt{s}}$, i.e., they depend of R (see Fig. 17 d). It follows that for $R < \sqrt{2}d_o$ they do not depend on the intrinsic parameter of the vortex.

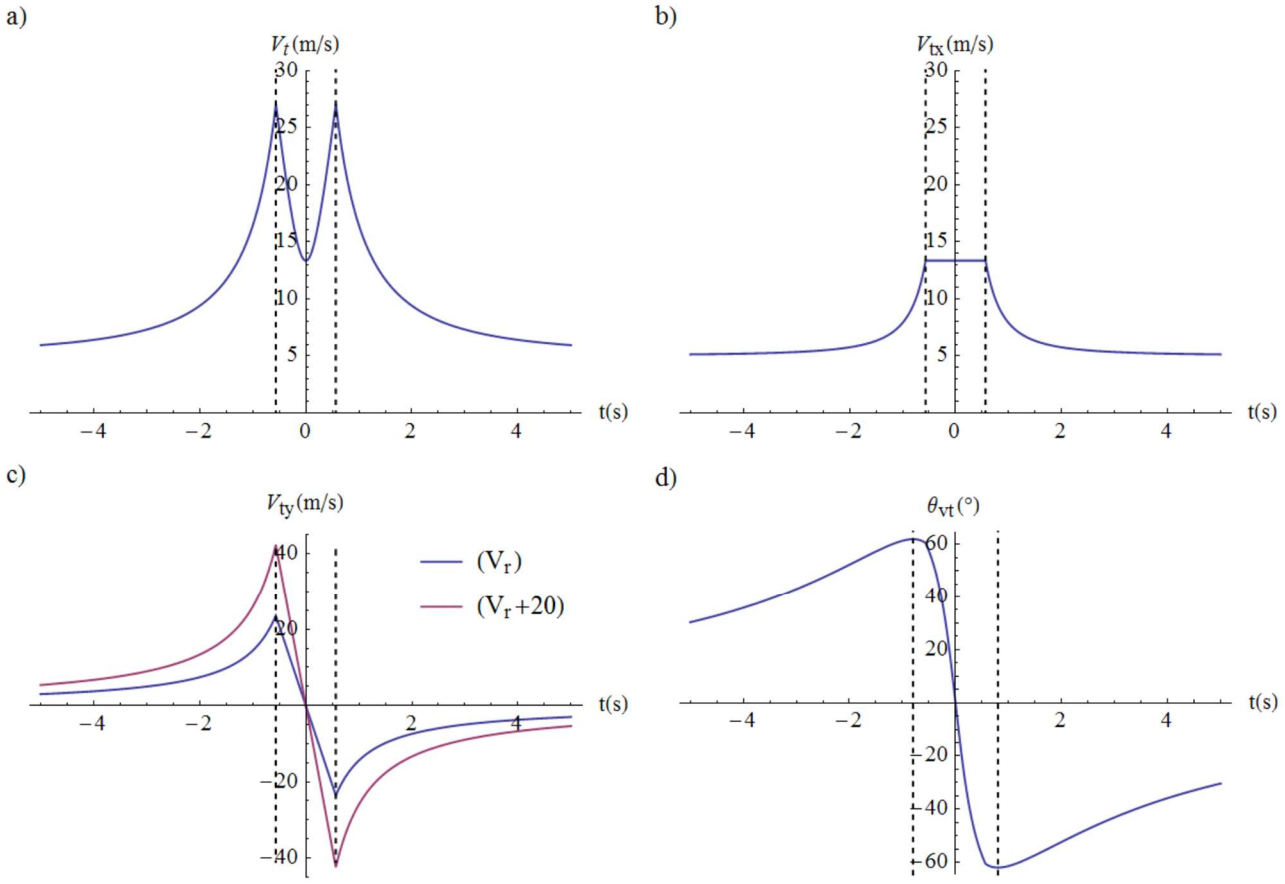

Fig. 17 *Wind signatures of a dust devils that has a direct passage on the meteorological station in case of concordant rotation. The dust devil depicted in blue has the following parameters: $s = 5$ m/s , $\theta_s = 0$, $V_r = 25$ m/s, $R = 3$ m , $d_o = 1$ m. The four plots are: a)the total wind speed v_t; b) the x-axis component of v_t; c) the y-axis component of v_t; d) the direction of v_t. The dashed lines indicate the position of the maximum and of the minimum of the functions. In c) we also show how the position of the maximum and minimum is the same for dust devils of different intrinsic rotational speed (20 m/s faster rotation).*

A.2 Discordant Rotation

Similarly to the concord rotation case, we first derive the trends of the components of the total velocity of the vortex during its passage over the station. Substituting eq.(1b) in eqs. (23) and (24) we get:

$$v_{tx}(d) = s - V_r \frac{d_o}{R} \tag{32}$$

$$\mathrm{v}_{ty}(d) = -V_r \frac{d}{R} \sqrt{1 - \left(\frac{d_o}{d}\right)^2} \quad \textbf{(33)}$$

Also in this case v_{tx} is constant for the entire duration of the passage. The stationary points of v_{ty} are in $d = \pm\sqrt{2}\, d_o$ ($t = \pm\frac{d_o}{s}$) for $R < \sqrt{2}d_o$, and in $d = \pm R$ ($t = \pm\frac{\sqrt{R^2 - {d_o}^2}}{s}$) for $R > \sqrt{2}d_o$. The total velocity has two maxima in $d = \pm R$ ($t = \pm\frac{\sqrt{R^2 - {d_o}^2}}{s}$), and the direction $\theta_{vt}(d)$ assumes maximum and minimum values in $d = \pm\frac{d_o\sqrt{|2s+w|}}{\sqrt{s}}$ ($t = \pm\frac{d_o\sqrt{|s+w|}}{\sqrt{s^2}}$) for $R < \frac{d_o\sqrt{|2s+w|}}{\sqrt{s}}$, and in $d = \pm R$ ($t = \pm\frac{\sqrt{R^2 - {d_o}^2}}{s}$) for $R > \frac{d_o\sqrt{|2s+w|}}{\sqrt{s}}$. Similarly to the previous sections, we show in Fig. 18 the trends of $\mathrm{v}_t(t)$, its components v_{tx} and v_{ty} and its direction $\theta_{vt}(d)$ for a dust devil with parameters defined in Fig. 5 and passing 1 m from the station ($d_o = 1\, m$), to allow for easy comparison with the previous cases. Note that, as in the case of Fig. 17 b, in Fig. 18 b v_{tx} remains constant in the central region because eq.(32) does not depends on the distance.

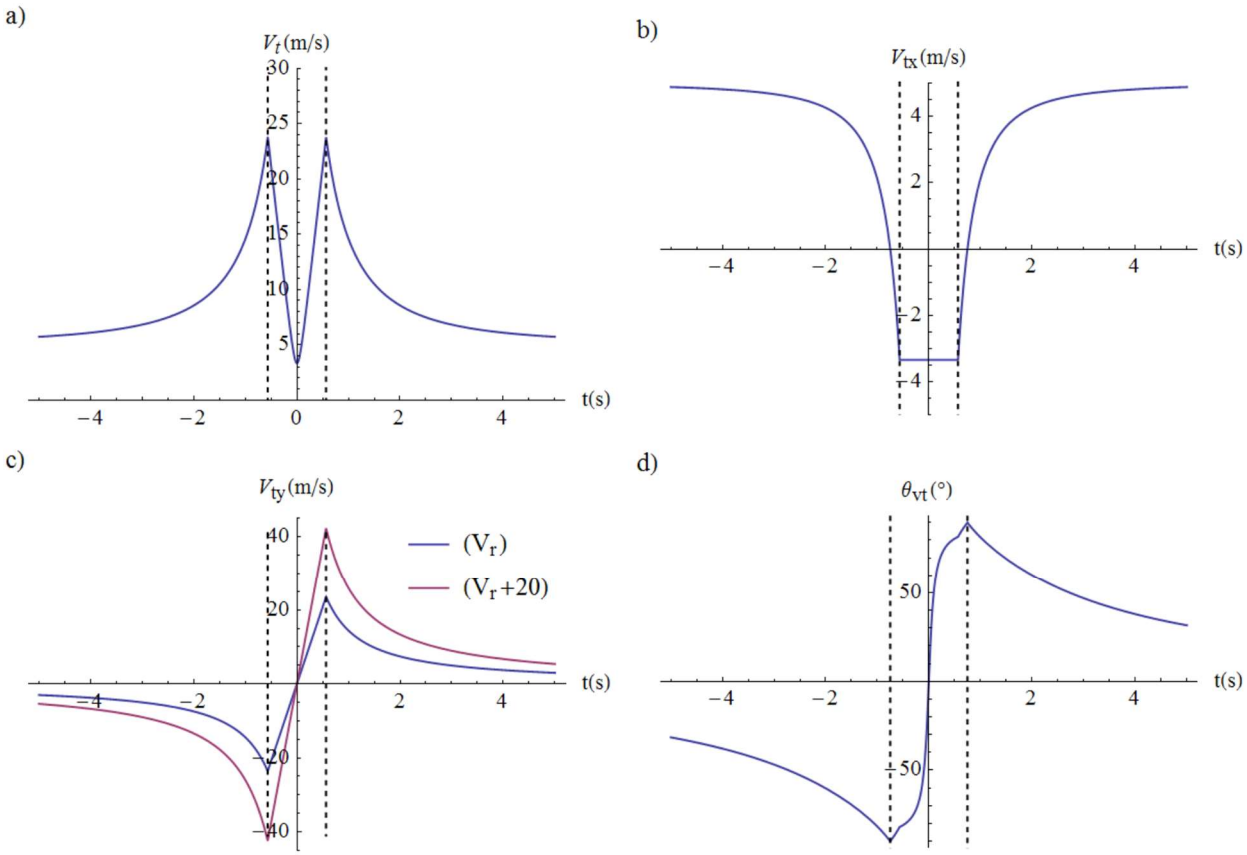

Fig. 18 *The time-trend of the measured wind velocity during the encounter of a discordantly rotating dust devil that passes over the fixed meteorological station. The dust devil depicted in blue has the following parameters: $s = 5$ m , $\theta_s = 0$, $V_r = 25$ m/s, $R = 3$ m , $d_o = 1$ m. The four plots are: a)the total wind speed v_t; b) the x-axis component of v_t; c) the y-axis component of v_t; d) the direction of v_t. The dashed lines indicate the position of the maximum and of the minimum of the functions. In c) the dust devils in red has a radius and a rotatory speed 1 m and 20 m/s greater than the blue one. Notice how the stationary points are still located in the same position.*

As for the case of non-direct passage, the trend of v_{ty} is opposite in case of concordant or discordant rotation. It is still possible to study the position of the critical points of v_{ty} (or θ_{vt}) in order to derive the impact parameter d_o, however, as show in Table 4, the situation is more complex and being this a direct passage ($d_o < R$) the knowledge of the distance is not of primary importance.

DIRECT PASSAGE	v_{ty} function	Maximum and Minimum position	
		$R < \sqrt{2}d_o$	$R > \sqrt{2}d_o$
Concordant rotation	$v_{ty}(d) = V_r \frac{d}{R} \sqrt{1 - \left(\frac{d_o}{d}\right)^2}$	$t = \mp \frac{d_o}{s}$	$t = \mp \frac{\sqrt{R^2 - {d_o}^2}}{s}$

Discordant rotation	$v_{ty}(d) = -V_r \frac{d}{R} \sqrt{1-\left(\frac{d_o}{d}\right)^2}$	$t = \pm \frac{d_o}{s}$	$t = \pm \frac{\sqrt{R^2 - {d_o}^2}}{s}$

Table 4 The functional form of v_{ty} in case of a direct passage of the event. The trend is the opposite in case of concordant and discordant rotation. The position of its critical points is shown. For $R < \sqrt{2}d_o$ this position is independent on R, hence can be directly used to infer the impact parameter d_o.

APPENDIX - B

Initial parameter estimation for the image processing

We report in Fig. 19 the collection of points whose distances from the station has been measured and that we have used use for our initial parameter evaluation.

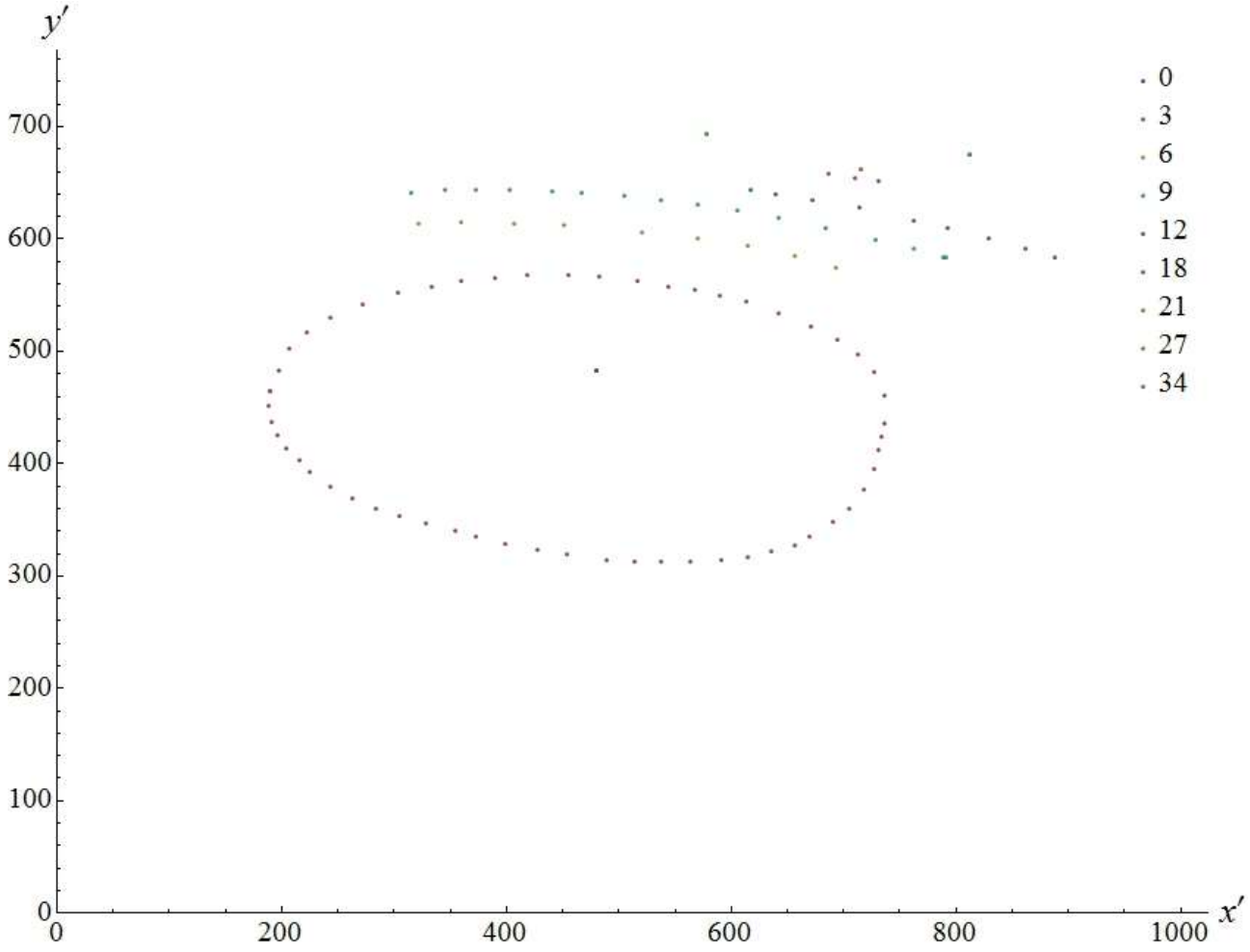

Fig. 19 ***The ensemble of marked points in the system O'x'y' used for the map fitting. The distances are in meters, the units of axes are in pixels.***

Before we proceed with the fitting of the 9 parameters (a_{ij}, b_i, c_i, d), we have to find an appropriate initial parameters. For this purpose, using polar coordinates, we fitted an ellipse onto the points closer to the meteorological station, i.e. those at 3m from it. We then transformed the resulting equation in Cartesian coordinates, obtaining:

$$A_o\, x'^2 + B_o\, x'y' + C_o y'^2 + D_o\, x' + E_o\, y' + F_o\ = 0 \tag{34}$$

Since in *Oxy* the points at 3 m lie along a circle, they satisfy:

$$x^2 + y^2 - R^2 = 0 \tag{35}$$

Eq.**Errore. L'origine riferimento non è stata trovata.**) is related to eq.**Errore. L'origine riferimento non è stata trovata.**) by mean of the transformation T(x,y) defined in eq. (28). Hence, substituting x' and y' in eq.**Errore. L'origine riferimento non è stata trovata.**) as per eq.(28), we get:

$$A\, x^2 + B\, xy + Cy^2 + D\, x + E\, y + F\ = 0 \tag{36}$$

Comparing eq. (35) and eq. (36) we get:

$$\begin{cases} A = 1 \\ B = 0 \\ C = 1 \\ D = 0 \\ E = 0 \\ F = -R^2 \end{cases} \tag{37}$$

From the images (see f.e. Fig. 8) one can also find the coordinates (x'_c, y'_c) of the origin of *Oxy* in *O'x'y'*:

$$\begin{cases} x'_c = T_x(0,0) = \dfrac{b_1}{d} \\ y'_c = T_y(0,0) = \dfrac{b_2}{d} \end{cases} \tag{38}$$

Adding to eqs. **Errore. L'origine riferimento non è stata trovata.** and **Errore. L'origine riferimento non è stata trovata.** a scaling relation $a_{11}=a_{22}$, we get a system of 9 equations in 9 parameters (a_{ij}, b_i, c_i, d). The additional constraint $a_{11}=a_{22}$ will be relaxed in the next section. Let us call $({a_{ij}}^V, {b_i}^V, {c_i}^V, d^V)$ the solution of the system. Despite this solution being satisfactory only for

690 points close to the station (see Fig. 20), it can be used as starting point for the fitting procedure
691 described in sect 1.3.1.

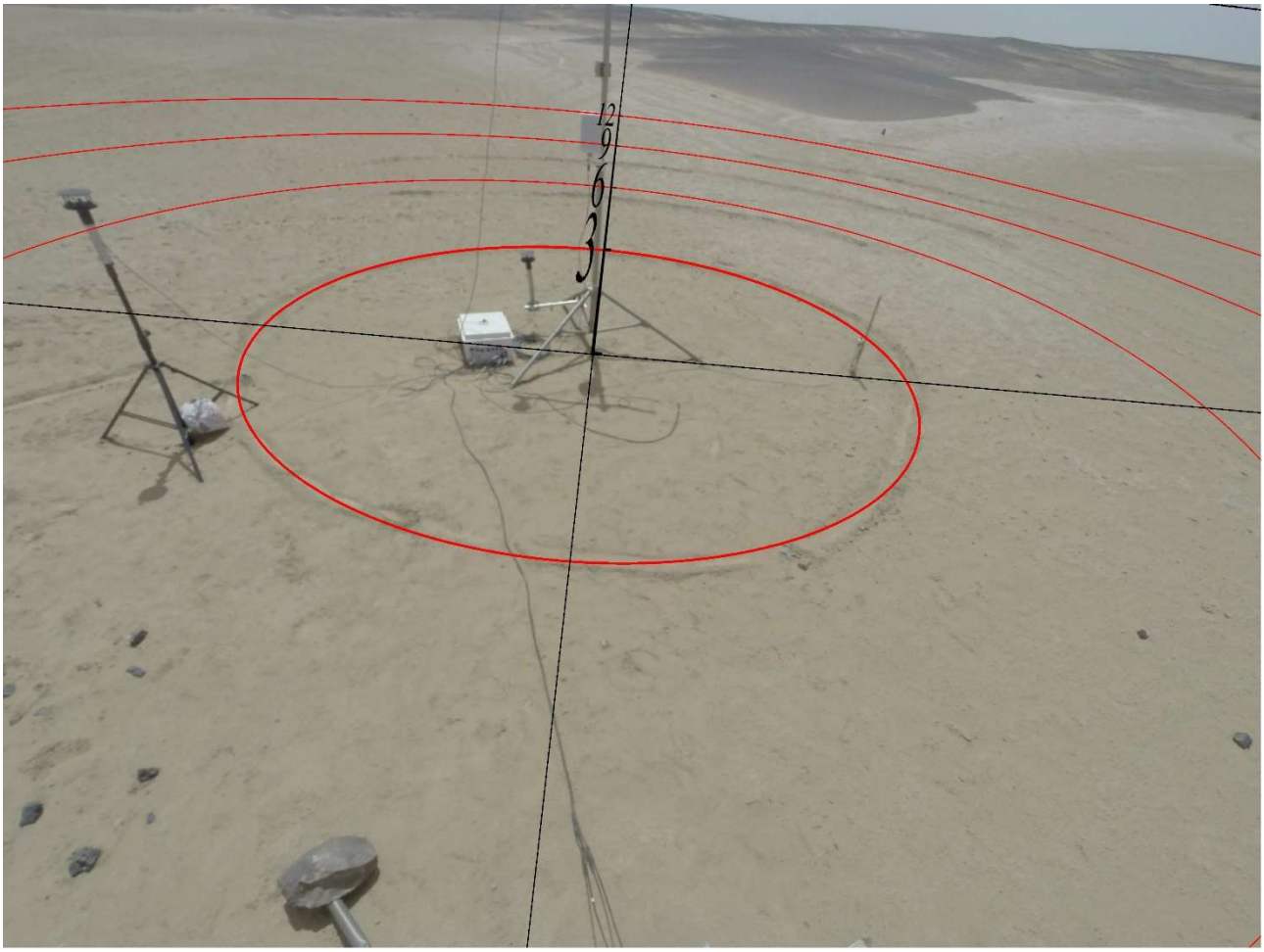

692

693 **Fig. 20** ***The result of our first step of the map fitting. The circles of radii 3,6,9 and 12 meters are plotted in red, while the axis and***
694 ***the line of horizon (top-right corner) are in black. The match between the red circles and the marked points is still poor farther***
695 ***than 3 meters from the station.***

696

697

698 ## Acknowledge

699 This work has been financed through the first call of the EuroPLANET 2020 research infrastructure
700 and performed with the collaboration of the IBN Battuta centre.

References

Aguirre, C., Franzese, G., Esposito, F., Vazquez, L., Caro-Carretero, R., Vilela-Mendes, R., ... & Popa, C. I. (2017). Signal-adapted tomography as a tool for dust devil detection. *Aeolian Research*, *29*, 12-22.

Atreya, S. K., Adams, E. Y., Niemann, H. B., Demick-Montelara, J. E., Owen, T. C., Fulchignoni, M., ... & Wilson, E. H. (2006). Titan's methane cycle. *Planetary and Space Science*, *54*(12), 1177-1187.

Balme, M., & Greeley, R. (2006). Dust devils on Earth and Mars. *Reviews of Geophysics*, *44*(3).

Balme, M. R., Pathare, A., Metzger, S. M., Towner, M. C., Lewis, S. R., Spiga, A., ... & Michaels, T. I. (2012). Field measurements of horizontal forward motion velocities of terrestrial dust devils: towards a proxy for ambient winds on Mars and Earth. *Icarus*, *221*(2), 632-645.

Bourke, M. C., K. S. Edgett, and B. A. Cantor (2008), Recent aeolian dune change on Mars, *Geomorphology*, 94, 247–255, doi:10.1016/j.geomorph.2007.05.012.

Cantor, B. A., Kanak, K. M., & Edgett, K. S. (2006). Mars Orbiter Camera observations of Martian dust devils and their tracks (September 1997 to January 2006) and evaluation of theoretical vortex models. *Journal of Geophysical Research: Planets*, *111*(E12).

Ellehoj, M. D., Gunnlaugsson, H. P., Taylor, P. A., Kahanpää, H., Bean, K. M., Cantor, B. A., ... & Holstein-Rathlou, C. (2010). Convective vortices and dust devils at the Phoenix Mars mission landing site. *Journal of Geophysical Research: Planets*, *115*(E4).

721 Edgett, K. S., & Malin, M. C. (2000). New views of Mars eolian activity, materials, and surface
722 properties: Three vignettes from the Mars Global Surveyor Mars Orbiter Camera. *Journal of*
723 *Geophysical Research: Planets*, *105*(E1), 1623-1650.

724 Esposito, F., Molinaro, R., Popa, C. I., Molfese, C., Cozzolino, F., Marty, L., ... & Ori, G. G. (2016).
725 The role of the atmospheric electric field in the dust-lifting process. *Geophysical Research Letters*,
726 *43*(10), 5501-5508.

727 Esposito, F., Debei, S., Bettanini, C., Molfese, C., Rodríguez, I. A., Colombatti, G., ... & Schipani, P.
728 (2018). The DREAMS experiment onboard the Schiaparelli module of the ExoMars 2016 mission:
729 design, performances and expected results. *Space Science Reviews*, *214*(6), 103.
730
731 Farrell, W.M., McLain, J.L., Collier, M.R., Keller, J.W., 2017. The Martian dust devil electron
732 avalanche: laboratory measurements of the E-field fortifying effects of dust-electron absorption.
733 Icarus297, 90–96.
734
735 Farrell, W. M., McLain, J. L., Collier, M. R., & Keller, J. W. (2017). The Martian dust devil electron
736 avalanche: Laboratory measurements of the E-field fortifying effects of dust-electron absorption.
737 *Icarus*, *297*, 90-96.

738 Fenton, L., Reiss, D., Lemmon, M., Marticorena, B., Lewis, S., & Cantor, B. (2016). Orbital
739 observations of dust lofted by daytime convective turbulence. *Space Science Reviews*, *203*(1-4), 89-
740 142.

741 Ferri, F., Smith, P. H., Lemmon, M., & Renno, N. O. (2003). Dust devils as observed by Mars
742 Pathfinder. *Journal of Geophysical Research: Planets*, *108*(E12).

743 Fisher, J. A., Richardson, M. I., Newman, C. E., Szwast, M. A., Graf, C., Basu, S., ... & Wilson, R.
744 J. (2005). A survey of Martian dust devil activity using Mars Global Surveyor Mars Orbiter Camera
745 images. *Journal of Geophysical Research: Planets*, *110*(E3).

746 Franzese, G., Esposito, F., Lorenz, R., Silvestro, S., Popa, C. I., Molinaro, R., ... & Deniskina, N.
747 (2018). Electric properties of dust devils. *Earth and Planetary Science Letters*, *493*, 71-81.

748 Giaiotti, D. B., & Stel, F. U. L. V. I. O. (2006). The Rankine vortex model. *October. University of*
749 *Trieste*.

750 Greeley, R., Balme, M. R., Iversen, J. D., Metzger, S., Mickelson, R., Phoreman, J., & White, B.
751 (2003). Martian dust devils: Laboratory simulations of particle threshold. *Journal of Geophysical*
752 *Research: Planets*, *108*(E5).

753 Guzewich, S. D., Toigo, A. D., Kulowski, L., & Wang, H. (2015). Mars Orbiter Camera climatology
754 of textured dust storms. *Icarus*, *258*, 1-13.

755 Harrison, R. G., Barth, E., Esposito, F., Merrison, J., Montmessin, F., Aplin, K. L., ... & Houghton,
756 I. M. P. (2016). Applications of electrified dust and dust devil electrodynamics to Martian
757 atmospheric electricity. *Space Science Reviews*, 1-47.

758 Klose, M., Jemmett-Smith, B.C., Kahanpää, H., Kahre, M., Knippertz, P., Lemmon, M.T., Lewis,
759 S.R., Lorenz, R.D., Neakrase, L.D. V., Newman, C., Patel, M.R., Reiss, D., 2016.
760

761 Levenberg, K. "A Method for the Solution of Certain Problems in Least Squares." *Quart. Appl. Math.*
762 **2**, 164-168, 1944.

763 Lorenz, R.D. (2016). *Heuristic estimation of dust devil vortex parameters and trajectories from*
764 *single-station meteorological data: application to insight at Mars. Icarus271, 326–337.*

765

766 Malin, M. C., & Edgett, K. S. (2001). Mars global surveyor Mars orbiter camera: interplanetary cruise
767 through primary mission. *Journal of Geophysical Research: Planets*, *106*(E10), 23429-23570.

768 Marquardt, D. "An Algorithm for Least-Squares Estimation of Nonlinear Parameters." *SIAM J. Appl.*
769 *Math.* **11**, 431-441, 1963.

770 Murphy, J. R., & Nelli, S. (2002). Mars Pathfinder convective vortices: Frequency of occurrence.
771 *Geophysical research letters*, *29*(23).

772 Murphy, J., Steakley, K., Balme, M., Deprez, G., Esposito, F., Kahanpää, H., ... & Patel, M. (2016).
773 Field measurements of terrestrial and martian dust devils. *Space Science Reviews*, *203*(1-4), 39-87.

774 Neakrase, L. D. V., Balme, M. R., Esposito, F., Kelling, T., Klose, M., Kok, J. F., ... & Wurm, G.
775 (2016). Particle lifting processes in dust devils. *Space Science Reviews*, *203*(1-4), 347-376.

776 Neubauer, F. M. (1966). Thermal convection in the Martian atmosphere. *Journal of Geophysical*
777 *Research*, *71*(10), 2419-2426.

778

779 Rankine, W.J.M. A Manual of Applied Mechanics; C. Griffin and Co., Limited: London, UK, 1901.
780

781 Ringrose, T. J., Towner, M. C., & Zarnecki, J. C. (2003). Convective vortices on Mars: a reanalysis
782 of Viking Lander 2 meteorological data, sols 1–60. *Icarus*, *163*(1), 78-87.

783 Silvestro, S., Fenton, L. K., Vaz, D. A., Bridges, N. T., & Ori, G. G. (2010). Ripple migration and
784 dune activity on Mars: Evidence for dynamic wind processes. *Geophysical Research Letters*, *37*(20).

785 Silvestro, S., Vaz, D. A., Di Achille, G., Popa, I. C., & Esposito, F. (2015). Evidence for different
786 episodes of aeolian construction and a new type of wind streak in the 2016 ExoMars landing ellipse
787 in Meridiani Planum, Mars. *Journal of Geophysical Research: Planets*, *120*(4), 760-774.
788
789 Sinclair, P. C. (1964). Some preliminary dust devil measurements. *Mon. Weather Rev*, *22*(8), 363-
790 367.
791
792 Sinclair, P. C. (1969). General characteristics of dust devils. *Journal of Applied Meteorology*, *8*(1),
793 32-45.
794
795 Sinclair, P. C. (1973). The lower structure of dust devils. *Journal of the Atmospheric Sciences*, *30*(8),
796 1599-1619.
797
798 Spiga, A., Banfield, D., Teanby, N. A., Forget, F., Lucas, A., Kenda, B., ... & Garcia, R. F. (2018).
799 Atmospheric science with InSight. *Space Science Reviews*, *214*(7), 109.

800 Stanzel, C., Pätzold, M., Williams, D. A., Whelley, P. L., Greeley, R., Neukum, G., & HRSC Co-
801 Investigator Team. (2008). Dust devil speeds, directions of motion and general characteristics
802 observed by the Mars Express High Resolution Stereo Camera. *Icarus*, *197*(1), 39-51.

803 Thomas, P., & Gierasch, P. J. (1985). Dust devils on Mars. *Science*, *230*(4722), 175-177.

804 Whelley, P. L., & Greeley, R. (2008). The distribution of dust devil activity on Mars. *Journal of*
805 *Geophysical Research: Planets*, *113*(E7).
806